

Lunar phase function at 1064 nm from Lunar Orbiter Laser Altimeter passive and active radiometry

M.K. Barker^{a,*}, X. Sun^b, E. Mazarico^b, G.A. Neumann^b, M.T. Zuber^c,
D.E. Smith^c

^a*Sigma Space Corporation, 4600 Forbes Blvd., Lanham MD 20706*

^b*Goddard Space Flight Center, 8800 Greenbelt Rd., Greenbelt, MD 20771*

^c*Dept. of Earth, Atmospheric and Planetary Sciences, MIT, 77 Massachusetts Ave.
Cambridge, MA 02139*

Abstract

10 We present initial calibration and results of passive radiometry collected by the
Lunar Orbiter Laser Altimeter onboard the Lunar Reconnaissance Orbiter over
the course of 12 months. After correcting for time- and temperature-dependent
dark noise and detector responsivity variations, the LOLA passive radiometry
measurements are brought onto the absolute radiance scale of the SELENE
15 Spectral Profiler. The resulting photometric precision is estimated to be $\sim 5\%$.
We leverage the unique ability of LOLA to measure normal albedo to explore
the 1064 nm phase function's dependence on various geologic parameters. On
a global scale, we find that iron abundance and optical maturity (quantified by
FeO and OMAT) are the dominant controlling parameters. Titanium abundance
20 (TiO₂), surface roughness on decimeter to decameter scales, and soil thermo-
physical properties have a smaller effect, but the latter two are correlated with
OMAT, indicating that exposure age is the driving force behind their effects
in a globally-averaged sense. The phase function also exhibits a dependence
on surface slope at ~ 300 m baselines, possibly the result of mass wasting
25 exposing immature material and/or less space weathering due to reduced sky
visibility. Modeling the photometric function in the Hapke framework, we find
that, relative to the highlands, the maria exhibit decreased backscattering, a
smaller opposition effect (OE) width, and a smaller OE amplitude. Immature
highlands regolith has a higher backscattering fraction and a larger OE width
30 compared to mature highlands regolith. Within the maria, the backscattering
fraction and OE width show little dependence on TiO₂ and OMAT. Variations
in the phase function shape at large phase angles are observed in and around the
Copernican-aged Jackson crater, including its dark halo, a putative impact melt
deposit. Finally, the phase function of the Reiner Gamma Formation behaves
35 more optically immature than is typical for its composition and OMAT, suggest-
ing the visible-to-near-infrared spectrum and phase function respond differently
to the unusual regolith evolution and properties at this location.

Keywords: Photometry, Moon, surface, Regoliths

*Corresponding author
Preprint submitted to Elsevier
Email address: michael.k.barker@nasa.gov (M.K. Barker)

1. Introduction

40 The reflectance of the Moon is a fundamental property of the surface that holds clues to the Moon’s formation and evolution (Heiken et al., 1991; Lucey, 2006) because it is closely linked to composition and mineralogy. The reflectance also depends on such physical properties of the regolith as compaction state, surface roughness, particle size, shape, presence of grain surface asperities, sub-
45 surface fractures, coatings, inclusions, etc., all of which can be correlated with composition and mineralogy (McGuire and Hapke, 1995; Lucey, 2006; Shepard and Helfenstein, 2007). These chemical and physical properties of the regolith are also modified by space weathering, the collective action of bombardment by micrometeorites, energetic particles, and electromagnetic radiation (Gault et al.,
50 1974; Hapke, 2001). Accurate interpretation of surface reflectance depends on viewing/illumination geometry, which can vary systematically between observations and instruments (Besse et al., 2013b; Mustard and Pieters, 1989), as well as on the aforementioned regolith properties. The viewing/illumination geometry consists of three key angles: incidence angle (i), the angle between the
55 surface-to-light-source and surface normal vectors, emission angle (e), the angle between the surface normal and surface-to-observer vectors, and phase angle (g), the angle between the surface-to-light-source and surface-to-observer vectors. The so-called photometric function describes how the reflectance depends on viewing/illumination geometry while the phase function is the part of the
60 photometric function that quantifies the phase-angle dependence in particular (Hapke, 2012b).

The multitude of lunar orbiting spacecraft data, ground-based telescopic observations, laboratory measurements of returned and simulated regolith samples, and continuously advancing remote sensing techniques over the last half-century
65 have improved our knowledge and understanding of the lunar photometric function. Knowledge of the photometric function is required to properly correct observations to a standard viewing/illumination geometry for comparison and analysis, and several studies have derived photometric corrections for specific datasets facilitating their mosaicing for color ratio maps and enabling more reliable
70 synthesis of data from multiple instruments (e.g., McEwen, 1996; Buratti et al., 2011; Yokota et al., 2011; Besse et al., 2013a; Sato et al., 2014). This photometric correction can include an empirical model of the phase function, such as a polynomial (Buratti et al., 2011; Besse et al., 2013b), or a theoretically-based model, such as the Hapke model (Hapke, 2012b, and references therein)
75 or the Shkuratov model (Shkuratov et al., 1999).

The phase function is also of interest for better understanding the geologic and space weathering influences on regolith characteristics. However, it is not clear yet whether one can uniquely determine such characteristics from the observed phase function alone given the complex mix of particle properties and
80 evolutionary processes applicable to planetary regolith, and the fact that multiple combinations of i and e can have the same phase angle. (Shepard and Helfenstein, 2007; Helfenstein and Shepard, 2011; Souchon et al., 2011; Cord et al., 2003). Spatial variations in the lunar phase function have been found

that are correlated with geologic context, most notably between the maria and
85 highlands (Kreslavsky et al., 2000; Buratti et al., 2011; Yokota et al., 2011; Sato
et al., 2014), but also at other locations with special geologic characteristics,
such as the Reiner Gamma Formation (Kreslavsky et al., 2000; Kreslavsky and
Shkuratov, 2003; Kaydash et al., 2009) and pyroclastic deposits in the Lavoisier
crater area (Souchon et al., 2013). Several studies have used phase ratio images,
90 the ratio between two images of the same location taken at different phase an-
gles. Variations in this ratio are usually interpreted as changes in the physical
structure of the regolith, like the surface roughness or porosity (Kreslavsky and
Shkuratov, 2003; Kaydash et al., 2009). Another approach is to fit a theoretical
model to measurements of the phase function at a wide range of phase angles.
95 For example, Sato et al. (2014) used 21 months of observations with the Lunar
Reconnaissance Orbiter (LRO) Wide Angle Camera (WAC) to study the wave-
length and spatial dependence of Hapke model parameters in the ultraviolet-to-
visible (UV-VIS) spectral range. They found that the highlands phase function
was more backscattering than that of the maria, which they interpreted to be
100 the result of a larger fraction of agglutinates formed from high-albedo silicates
in the highlands compared to the maria, and a higher fraction of submicroscopic
metallic iron (SMFe) and opaque minerals (like ilmenite) in the maria compared
to the highlands. They also found that the opposition effect (OE; the surge in
brightness at phase angles approaching zero) was wider for immature highlands
105 regolith than mature highlands regolith, which they tentatively attributed to
variations in grain size distribution.

The goal of the present work is to further elucidate the phase function be-
havior in the near-IR, especially with respect to geologic context. Our primary
dataset consists of reflectance measurements made by the Lunar Orbiter Laser
110 Altimeter (LOLA) aboard LRO. In addition to its primary altimetric measure-
ments mapping lunar topography (Smith et al., 2010b), this instrument mea-
sures surface reflectance at 1064 nm with two complementary methods. The
first method uses the ratio of the surface-backscattered and transmitted laser
pulse energies. This active radiometry measures the zero-phase reflectance, or
115 normal albedo (A_n), which is independent of topography. Lucey et al. (2014)
presented an analysis and global maps of A_n from active radiometry collected
during the nominal mapping phase, and Lemelin et al. (2015, this issue) derive
an improved normal albedo calibration and maps, which we use in this study.

Although not in the original instrument mission goals, we have also recently
120 developed a second reflectance measurement technique, which turns the LOLA
noise monitoring house-keeping data into a unique passive radiometry science
measurement of the Moon. This dataset is unique because it covers a narrow
spectral band, it is as precisely geolocated as the altimetry data, and it com-
plements the normal albedo measurement made with the laser. With passive
radiometry, the instrument measures the number of solar photons reflected off
125 the surface, which depends on the topography and viewing/illumination geom-
etry. In this paper, we focus on the passive radiometry, but we leverage the
unique ability of LOLA to measure the phase function over all phase angles
including zero degrees. While passive imagers can make observations at zero

130 phase, these measurements are very limited spatially (typically confined close to the equator). In contrast, the LOLA active radiometry yields zero-phase measurements over the whole surface, providing a more complete view of the photometric behavior than is typical with imagers.

This is not the first work to make use of a planetary laser altimeter as a 135 passive radiometer. The Mars Orbiter Laser Altimeter (MOLA) collected passive radiometry for ~ 6 years until contact with Mars Global Surveyor was lost. Sun et al. (2006) calibrated the MOLA passive radiometry and demonstrated its high stability and precision ($< 5\%$). This dataset was used to study the distribution and thickness of Martian water ice permafrost (Mitrofanov et al., 140 2007) and interannual and seasonal variations in residual ice cap albedo (Byrne et al., 2008).

This paper is organized as follows. In Section 2, we describe the instrument and data used. In Section 3, we describe the calibration of the data. In Section 4 and Section 5, we present the photometric function and phase function, 145 respectively, and compare the latter to previous determinations in the literature. In Section 6, we examine how the phase function varies with geologic context. Then, we model the phase function behavior with a Hapke model (Section 7). In Section 8, we derive a large-scale “phase difference” map of the Moon and examine the geologic variations in phase function that it reveals, with particu- 150 lar attention to Jackson crater and Reiner Gamma. Finally, we summarize the results and make concluding remarks in Section 9.

2. Instrument and Data Description

LRO entered lunar orbit in June 2009 followed by a commissioning phase during which the spacecraft had a $\sim 30 \times 200$ km polar orbit with periapsis near 155 the south pole. In September 2009, the spacecraft moved into a nearly circular 50 km, 2-hour orbit for the nominal mapping phase. In December 2011, it was moved into a quasi-stable elliptical orbit similar to the commissioning orbit.

LOLA is a time-of-flight laser altimeter operating at a wavelength of 1064 nm and a firing rate of 28 Hz (Smith et al., 2010a). A diffractive optical element 160 splits the laser beam into 5 separate far-field spots which form a cross pattern on the surface rotated by 26° with respect to the along-track direction. The 5 returned pulses enter the receiver telescope and are fed via 400 μ rad field-of-view fiber optic cables to 5 separate detector assemblies. Each assembly has a bandpass filter 0.8 nm wide centered on 1064 nm and a silicon avalanche 165 photodiode (APD). In the nominal mapping phase, the detector field-of-view around each 5-m-diameter laser spot on the surface was 20 m, and the spot centers were separated by 25 m, for a footprint diameter of ~ 50 m. In the present elliptical orbit, however, the field-of-view/footprint diameter range from $\sim 15/30$ m at periapse to $\sim 70/180$ m at apoapse. The LRO ground speed 170 has remained nearly unchanged at ~ 1.6 km s^{-1} , yielding a separation between successive shots of ~ 57 m on the surface.

LOLA continuously collects background noise triggers with a dedicated noise counter for each channel that reads out the number of triggers collected every

28th of a second. Hence, the effective exposure time for the passive radiometry is 0.0357 sec, which we refer to as a “shot.” During normal lunar laser ranging operations, the flight software keeps the noise detection probability at a very low level ($\sim 1\%$) by dynamically adjusting the return pulse detection threshold for each channel. In the passive mode, however, these background noise photons are the signal of interest so the thresholds are held fixed at much lower values to increase the signal. Only channels 2 – 5 are used in passive radiometry mode; channel 1 (the center spot) is not used because it also measures background light from the Earth as part of the one-way, Earth-to-LRO, laser ranging campaign (Zuber et al., 2010; Mao et al., 2013).

Since November 2013, LOLA has been collecting passive radiometry, mostly in the northern hemisphere, where the spacecraft altitude is too high for active lunar altimetric ranging. For the first ~ 6 months of operation, the passive mode was enabled at latitudes above $\sim 24^\circ$ N. Since then it has been operating above $\sim 3^\circ$ S. In addition, the passive mode operates during large ($\gtrsim 20^\circ$) spacecraft slews irrespective of latitude, and for the entire orbit when $|\beta|$ (the angle between the spacecraft angular momentum vector, the Moon’s center, and the Sun) is $\gtrsim 80^\circ$. The result is that 86% of all measurements lie above the equator and 95% have off-nadir angles $< 5^\circ$.

In this study, we use the passive data during the first year of operation, corresponding to ~ 4200 orbits from day of year 2009 (DOY₂₀₀₉) 1801 to 2156. Note that we define DOY₂₀₀₉ as a monotonically increasing time variable with a reference (DOY₂₀₀₉ = 0.0) of midnight on the first day of 2009. To account for the fact that the LRO mission extended beyond 2009, we let DOY₂₀₀₉ take higher values than 365. The passive mode operated with constant threshold for each channel, but two sets of gain values, which we refer to as Operation Modes (OMs) 1 and 2. These settings are listed in Table 1. All data were collected in OM 1 except during the OM 2 time periods of DOY₂₀₀₉ = 1883.02 – 1908.56 and 1935.01 – 1957.66.

Orbit determination was performed with the lunar gravity field GRGM900C from the Gravity Recovery and Interior Laboratory (GRAIL) mission (Zuber et al., 2013; Lemoine, 2014). With the GRAIL gravity field, the accuracy of the LRO reconstructed trajectory is ~ 10 m in total position and ~ 0.5 m vertically (Mazarico et al., 2013). To boost the signal-to-noise ratio (S/N), we use a 5-shot (0.18 sec or ~ 285 m) along-track moving average of channels 2 – 5 giving an effective pixel size $\sim 100 \times 300$ m. This yields 20 points per average and a final total of ~ 200 million data points for the considered time period.

3. Data Calibration

In this section, we describe the calibration procedure to account for time-, temperature-, and channel-dependent photoelectron noise and responsivity variations, and to transform the passive radiometry noise counts into an absolute radiometric value. The instrument noise counts consist of two parts, dark noise (baseline noise floor) and the photon noise, both of which are functions of detector temperature and subject to long-term drift. We used the nighttime data

Table 1: Threshold and gain settings for Operation Modes 1 and 2 (see text for details).

| Chan | Threshold (mV) | Gain |
|------|-------------------|-------|
| OM 1 | | |
| 2 | 12.9 | 49.10 |
| 3 | 13.3 | 50.00 |
| 4 | 11.8 | 50.90 |
| 5 | 14.2 | 50.70 |
| OM 2 | | |
| 2 | 12.9 | 49.87 |
| 3 | 13.3 | 50.00 |
| 4 | 11.8 | 49.23 |
| 5 | 14.2 | 50.16 |

to calibrate the model for the dark noise, and the sunlit Moon at fixed locations and viewing/illumination angles to radiometrically calibrate the photon noise. We expect the calibration uncertainties to improve with time as more data are collected.

3.1. Dark-current

Even in darkness, thermal electrons within the detector electronics give rise to a non-zero output. This dark current depends on detector temperature, which varies by several degrees throughout an entire orbit, and, to a much lesser extent, undergoes a long-term drift. The range of temperatures spanned by the night side data is similar to that spanned by the day side data, which allows us to determine this correction function using nighttime data. There is a slight increase in the dark current with time amounting to ~ 20 counts every 100 days. We model the dark current counts, C_d , for each channel separately by fitting the night side data from the entire year under study with a cubic function of detector temperature T with coefficients a_i and a linear time term with slope b_1 :

$$C_d = a_0 + a_1T + a_2T^2 + a_3T^3 + b_1\text{DOY}_{2009}. \quad (1)$$

Table 2 lists the best-fit model parameters for each channel. The differences in parameter values between the detectors are due to the different thresholds and gains (lower threshold or gain leads to higher or lower dark current, respectively), and the fact that each detector assembly has its own set of electrical components with unique characteristics. Figure 1 shows a 2-dimensional (2-D) histogram of the channel 2 full rate (pre-averaged) night side data and the best-fit temperature function for three different DOY_{2009} : 1800 (lower), 2000 (middle), and 2200 (upper). After subtracting the best-fit model for each channel, the RMS residual for the full-rate data is ~ 65 counts (Figure 2). The

Table 2: Parameters of dark-current model.

| Channel | a_0 | a_1 | a_2 | a_3 | b_1 |
|---------|----------|----------|--------|-------|-------|
| OM 1 | | | | | |
| 2 | -3443.12 | 875.42 | -38.24 | 0.58 | 0.19 |
| 3 | -7929.01 | 1509.69 | -69.66 | 1.09 | 0.14 |
| 4 | 6047.78 | -360.17 | 13.31 | -0.13 | 0.17 |
| 5 | 1207.14 | 277.81 | -13.08 | 0.24 | 0.16 |
| OM 2 | | | | | |
| 2 | 3627.99 | -120.94 | 1.12 | 0.07 | 1.19 |
| 3 | 15242.98 | -1436.46 | 54.68 | -0.65 | 0.14 |
| 4 | 10516.94 | -1129.11 | 46.52 | -0.61 | 0.49 |
| 5 | 624.36 | 192.07 | -9.58 | 0.18 | 0.58 |

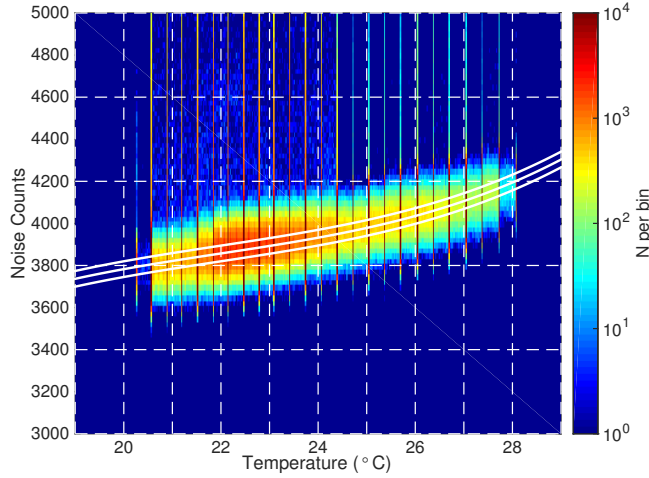


Figure 1: Channel 2 nighttime noise counts as a function of detector 2 temperature. The bin size is $0.025^\circ \text{C} \times 25$ counts. Best-fit dark-current model is plotted as a white line for three different DOY₂₀₀₉: 1800 (lower), 2000 (middle), and 2200 (upper). Each channel has its own model that is a cubic function of temperature and linear function of time (Table 2.)

standard deviation of the 5-shot averaged nighttime counts per orbit is ~ 20 . We subtract the dark current model from each channel's day side measurements to remove the thermal electron noise.

235 3.2. Responsivity

In addition to dark current thermal noise, each detector responds slightly differently to the same incident power. We account for this inter-channel responsivity variation by calculating the median counts ratio of channels 2, 4,

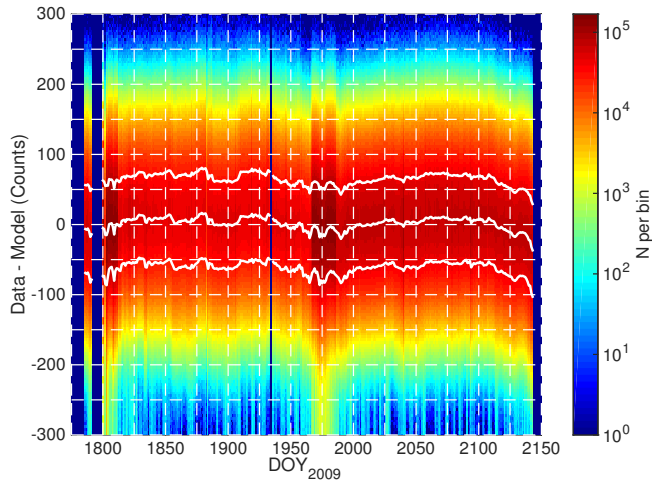


Figure 2: Residuals of best-fit dark-current models for all channels (defined as data - model) as a function of time. The bin size is 1 day \times 4 counts. The white lines show the mean and standard deviation per day.

and 5 relative to channel 3 for every orbit. Channel 3 was chosen as the reference channel because its gain was constant over the whole time period. Then, we model the ratios as separate linear functions of time and scale the day side counts for channels 2 – 5 accordingly. The best-fit y-intercept (a_0) and slope (a_1) are listed in Table 3. There is a small long-term time-dependence amounting to a responsivity change of 2 – 5% over the course of the year considered here. Figure 3 shows the residual daytime responsivity variation relative to channel 3 for every orbit after subtracting the best-fit linear functions of time. Some systematics remain, but cannot be easily described and corrected presently. The resulting RMS residual responsivity variation is 2% around unity. Gray shaded areas indicate the times when $|\beta| > 70^\circ$. At these high β values, there is increased noise in the estimation of the counts ratios due to the greater effects of shadows and low number statistics in the counts.

The detectors have a different temperature-dependent responsivity when light is incident upon them compared to when they are in the dark owing to the combined temperature dependence of the APD and the internal electronics. This requires a correction to the channel 3-normalized counts of all the channels as a function of channel 3 detector temperature. We take the approach of using the Moon itself as an absolute reference against which we can measure a daytime temperature dependence. To do so, we extract a photometrically uniform sub-sample from the entire dataset and plot the variation of counts relative to the mean in 1° -cubed bins of incidence, emission, and phase angle (i, e, g). The mean counts in each of these 3-D volume-elements (“voxels”) serves as the constant baseline against which any trend with temperature is measured. A voxel is an extension of the familiar 2-D pixel (picture-element) to 3-D (volume-

Table 3: Parameters of inter-channel responsivity correction.

| Chan | a_0 | a_1 |
|------|-------|------------------------|
| OM 1 | | |
| 2 | 1.40 | -1.44×10^{-4} |
| 4 | 1.19 | -7.18×10^{-5} |
| 5 | 1.58 | -5.72×10^{-5} |
| OM 2 | | |
| 2 | 1.37 | -1.44×10^{-4} |
| 4 | 1.28 | -7.18×10^{-5} |
| 5 | 1.28 | -5.72×10^{-5} |

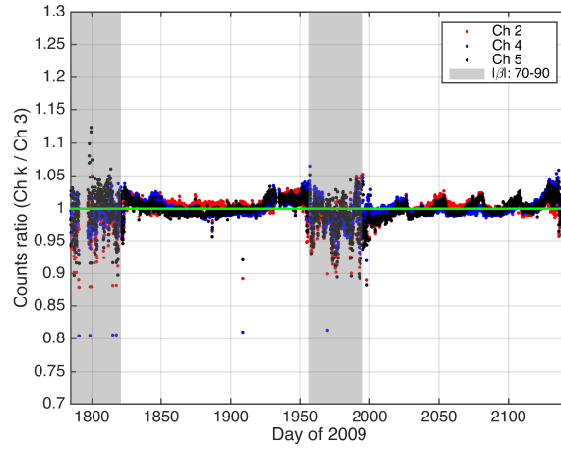


Figure 3: Daytime responsivity variation relative to channel 3 for every orbit after subtracting best-fit linear functions of time. The remaining RMS residual is 2%. Gray shaded areas indicate the times when $|\beta| > 70^\circ$.

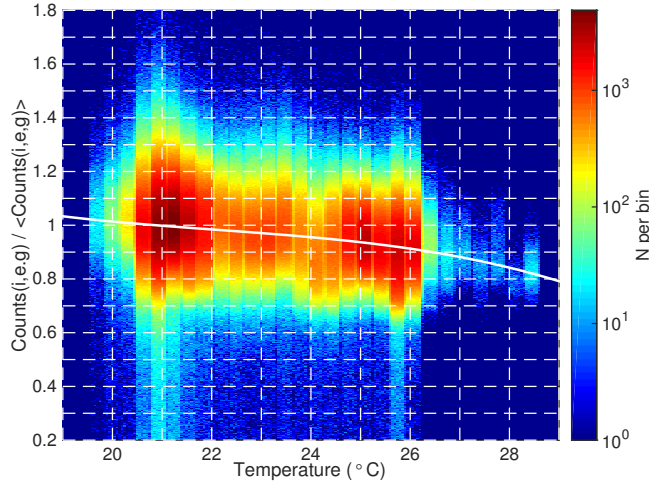


Figure 4: Fractional change in counts as a function of detector 3 temperature. The bin size is $0.05^\circ \text{ C} \times 0.001$. The white line is the best-fit cubic polynomial, which is used to remove the temperature dependence of the day side counts.

element). The sub-sample is chosen to minimize the range of counts expected in each voxel while keeping the number statistics high enough to probe the full range of temperature. We chose to focus on those points with $A_n = 0.25 - 0.35$ (encompassing the peak in the highlands' A_n distribution), latitudes $> 30^\circ$ (to ensure the full time period is sampled), $i < 75^\circ$ (to minimize the effect of shadows), and at least two points in their respective voxels (to avoid points that are the sole members of their voxels). The A_n values derived here and throughout this paper come from interpolating the LOLA measurement locations on the 4 pixel per degree (ppd) map presented by Lemelin et al. (2015, this issue). Figure 4 shows a 2-D histogram of $C(i, e, g) / \langle C(i, e, g) \rangle$, the deviation of each measurement's counts from the mean counts in its corresponding voxel, as a function of temperature for the highland sample. The white line is the best-fit cubic polynomial:

$$C(i, e, g) / \langle C(i, e, g) \rangle = 6.22694 - 0.68381T + 0.03020T^2 - 0.00045T^3. \quad (2)$$

After removing this temperature dependence, the daily average of $C / \langle C \rangle$ for the highland sample across the entire time period has a standard deviation of 5%. We take this as an estimate of the overall LOLA passive radiometry precision.

Figure 5 shows an example of the raw and corrected passive radiometry collected during one particular orbit on $DOY_{2009} = 2099$ with $\beta = 32^\circ$. The orbit starts on the night side, and as the spacecraft descends from the terminator-crossing near the north pole to the equator, the passive radiometry counts increase as the phase angle decreases. The counts follow the normal albedo modulated by the continuously changing viewing/illumination geometry and topography. After applying the corrections and 5-shot averaging described above, the

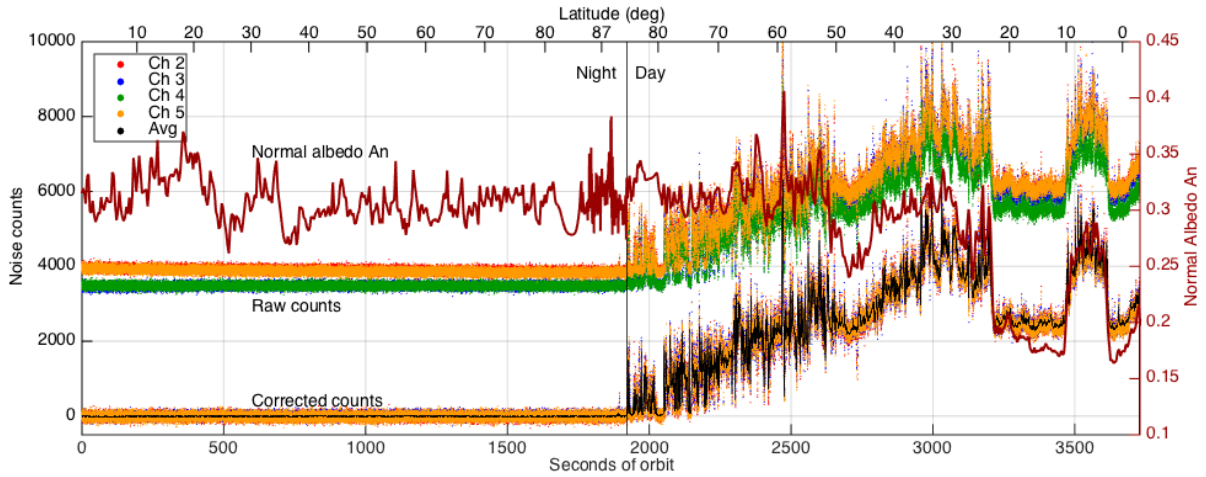


Figure 5: Passive radiometry collected during orbit 23834 at $\beta = 32^\circ$. The raw data and corrected data for channels 2 – 5 are both labeled and plotted in order of channel number. Black points show the 5-shot moving-average-filtered corrected data. The normal albedo along this ground track is also plotted as the brown line with scale given on the right-hand y-axis. The black vertical line marks the terminator crossing from night into day. The orbit starts at the ascending node with longitude $\lambda_0 = 238^\circ$ E.

counts (black points) are centered on zero during nighttime.

Figure 6 shows S/N as a function of phase angle for the entire dataset summed over all incidence and emission angles. The mean S/N and its standard deviation increase from $\sim 25 \pm 20$ at 85° to $\sim 300 \pm 100$ at 0° . Since the vast majority of observations were made at nadir, latitude is a proxy for the lowest phase observable at a given location. Here S/N is defined as the 20-point mean divided by the standard error of the mean (i.e., the standard deviation of the 20 counts divided by the square-root of 20). Therefore, it includes natural spatial variability as well as Poisson noise.

3.3. Radiance

To convert the LOLA noise counts to absolute radiance, we adopt the Spectral Profiler (SP) dataset as a reference. The SP was a line-scanning visible-to-IR spectrometer with a $\sim 500 \times 500$ m footprint onboard the Japanese SELENE (Kaguya) spacecraft. SELENE operated from November 2007 to April 2009 at an average altitude of 100 km, and from April 2009 to the planned lunar impact in July 2009 at an average altitude of 50 km. In December 2008, the failure of a reaction wheel forced Kaguya to rely on thrusters for pointing. We found that the SP data taken after the orbit was lowered were noticeably degraded, possibly due to orbit and attitude reconstruction problems related to the low altitude, the use of thrusters to control pointing, and the limited tracking data during the extended mission (Goossens et al., 2009), so these data were excluded from the calibration.

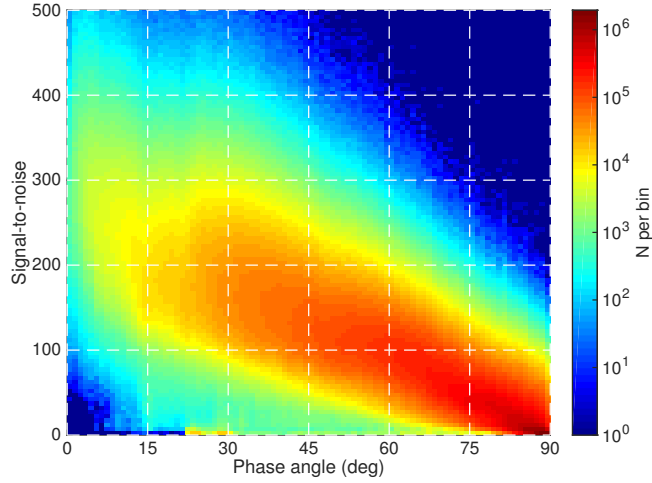


Figure 6: S/N ratio of 20-point along-track moving average for all ~ 200 million points as a function of phase angle. S/N is defined as the mean of the 20 points divided by the standard error of the mean. The bin size is $1^\circ \times 5$.

Figure 7 shows the radiance calibration to convert LOLA noise counts to absolute radiance. Approximately 2,700 points were matched between the LOLA and SP datasets at latitudes $0 - 35^\circ$ N and phase angles $0 - 55^\circ$, and the SP data were restricted to nadir pointing. To more easily see their density distribution in the figure, the points are plotted first as blue error bars and then as red points without error bars. Only LOLA points with emission angles $< 10^\circ$ were considered. To compute the viewing/illumination geometry of every LOLA measurement, we used the LOLA global 128 ppd digital elevation model (DEM; ~ 240 m at the equator, commensurate with the size of the moving average kernel applied to the raw passive radiometry). Each LOLA and SP measurement was also corrected for the Sun-Moon distance. Points were considered matches if they were located within 1 km of each other and had phase angle differences of $< 5^\circ$. To compute the SP radiance at 1064 nm, we linearly interpolated between the bracketing wavelengths of 1060 and 1068 nm.

The error bars were calculated to estimate spectral and spatial variation and Poisson noise. The SP error bars are the quadrature sum of two values: 1) the difference between the 1064-interpolated radiance of the matched point and next-closest point and 2) half the radiance difference between the bracketing spectral bands of the matched point. The LOLA error bars are the quadrature sum of 1) the counts difference between the matched point and next-closest point and 2) the matched point counts uncertainty as given by the standard error of the 20-point mean.

The relation between radiance and LOLA noise counts appears to be linear, so we solve for the best-fit slope and intercept in a least-squares sense following the method of York et al. (2004) to account for errors in both coordinates. The

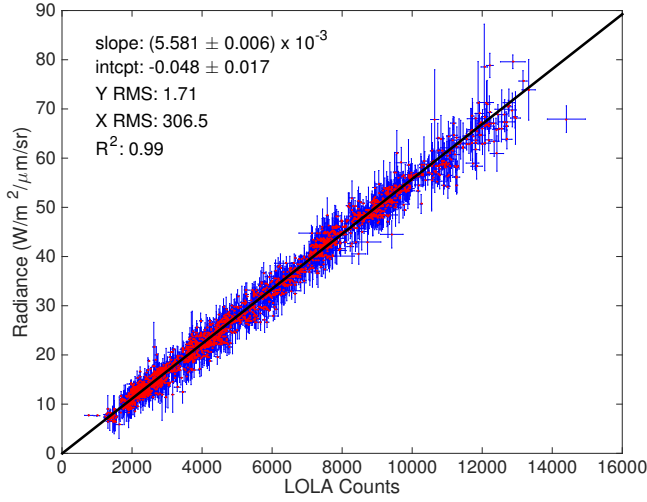


Figure 7: Radiance calibration to convert LOLA noise counts to absolute radiance. Approximately 2700 points were matched between the LOLA and SP datasets at nearby locations and similar viewing/illumination geometries. Error bars include spectral and spatial variation and Poisson noise.

resulting best-fit slope and intercept are $(5.581 \pm 0.006) \times 10^{-3}$ and -0.048 ± 0.017 , respectively. The best-fit model has an R^2 value of 0.99, an RMS radiance residual of 1.71 W/m²/μm/sr and RMS counts residual of 306.5. With this calibration, and taking 20 as the standard deviation of the night time noise counts, we estimate a 5σ detection limit of ~ 0.51 W/m²/μm/sr, well below the faintest data used for this calibration.

There is no obvious sign of non-linearity in Figure 7, but it is possible that departures from linearity could be below the noise level of the data or occur at radiances outside the range covered by the calibration. Most of the lunar surface has a near-IR $A_n < 0.4$ (Lucey et al., 2014), corresponding to a radiance of ~ 80 W/m²/μm/sr. Therefore, our calibration covers most of the range of expected radiances. Some very bright localized areas can have larger radiances, but they represent less than 0.01% of all the passive radiometry measurements. At the faint end, $\sim 10\%$ of the passive radiometry measurements with incidence angles $i < 80^\circ$ have radiances $\lesssim 5$ W/m²/μm/sr, and we take steps throughout the analysis to mitigate the topographic shadowing effects associated with higher incidence angles.

Finally, implicit in this procedure is the assumption that the SP absolute photometric accuracy is stable over time and signal strength. Yamamoto et al. (2011) analyzed 4 repeat observations of the Apollo 16 landing site taken at 6 month intervals between November 2007 and March 2009. They found that the reflectances after photometric correction showed differences of $\sim 0.4 - 1.1\%$, suggesting that the degradation of SP over that period was not significant. citet-

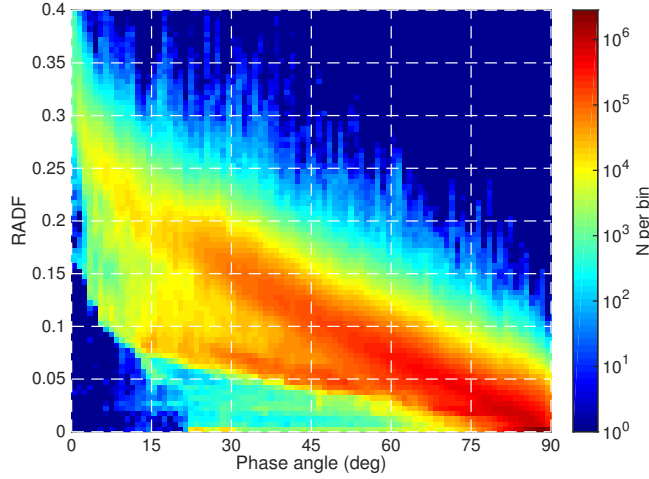


Figure 8: 2-D histogram of $RADF$ as a function of phase angle including all observed incidence and emission angle variation. The bin size is $1^\circ \times 0.005$. The upper and lower sequences correspond to the highlands and maria, respectively.

Pieters2013 compared the radiances measured by several instruments including SP and found generally good agreement between them, despite some deviations from one-to-one linearity of up to $\sim 20\%$, but the proportion of the deviations due to each instrument was unclear. Besse et al. (2013b) also compared SP data to several other instruments and concluded that the spectral slope of SP data was redder than the others, but that the absolute radiance was overestimated by only about 1% at 1064 nm. Therefore, it is likely that the absolute SP radiance is accurate at the $\sim 1\%$ level, but to be conservative, we adopt a systematic uncertainty of 20% for the fully calibrated LOLA passive radiometry.

3.4. Radiance Factor

Applying the corrections and calibration described above yields $I_0(i, e, g)$, the observed 1064 nm radiance at 1 AU. Then, every measurement is converted to radiance factor ($RADF$, also abbreviated as I/F in the literature) using the formalism of Hapke (2012b), which defines $RADF$ as the reflectance relative to a perfectly diffuse surface illuminated vertically:

$$RADF(i, e, g) = \pi I_0(i, e, g) / J_0, \quad (3)$$

where $J_0 = 647 \text{ W/m}^2/\mu\text{m}$ is the solar irradiance at 1064 nm. The 5σ detection limit above the dark noise corresponds to $RADF = 2.2 \times 10^{-3}$. The $RADF$ as a function of phase angle for the whole dataset (Figure 8) exhibits two distinct sequences corresponding to the highlands (upper) and maria (lower).

Figure 9 shows a 4 ppd map of A_n inferred from passive radiometry. To make this map, we divided each individual measurement's $RADF$ by the median

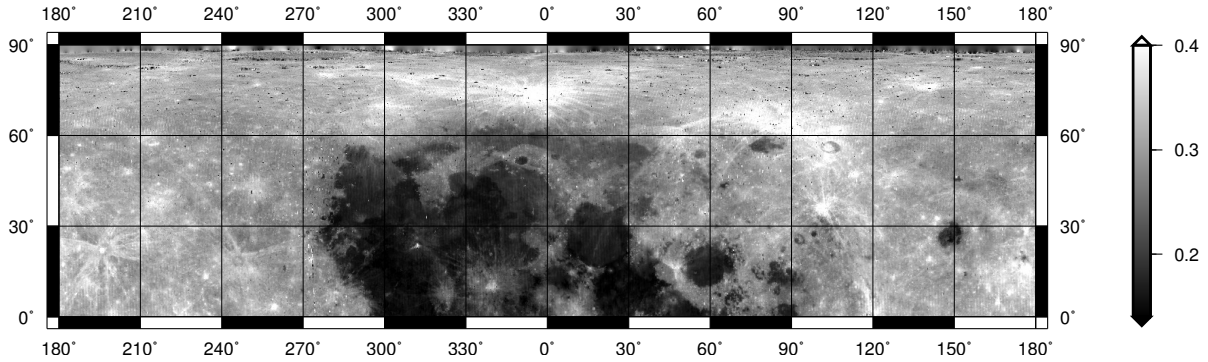


Figure 9: Cylindrical projection 4 ppd map of 1064 nm A_n from passive radiometry.

highlands *RADF* for its corresponding voxel. Then we regressed this quantity on the actively-derived A_n map after excluding $|\beta| > 70^\circ$ to minimize the effect of shadows. The resulting slope and y-intercept were 0.27 and 0.04, which can be loosely interpreted, respectively, as a globally-representative average albedo and the relative consistency of the passive and active photometric zero-points. The mean and standard deviation of the best-fit residuals were 0.0 ± 0.02 in *RADF* units. This serves as a useful confirmation of the overall fidelity of the passive radiometry.

4. Photometric Function

With the unique ability of LOLA to measure A_n with active radiometry and *RADF* with passive radiometry, we can correct every passive measurement for the local albedo of the surface by interpolating on the actively-derived 4 ppd A_n map of Lemelin et al. (2015, this issue). The resulting quantity, called the photometric function, is defined by the relation (Hapke, 2012b):

$$f(i, e, g) = \text{RADF}(i, e, g) / A_n, \quad (4)$$

and is displayed in Figure 10. It contains all the illumination and viewing geometry effects, which are linked to the regolith composition, structure, and grain properties, that act on the normal albedo to produce the passively-observed *RADF*. To our knowledge, this is the first time that the lunar photometric function on a global scale has been revealed by observational data alone. The maria and highlands sequences visible in Figure 8 have almost merged into one; there is still some distinction between them, which we examine further in Section 7, which describes Hapke modeling of various sub-samples of the data plotted in Figure 10. By definition, the photometric function should equal unity at zero phase. Indeed, the mode of the observed photometric function in the phase range $0 - 1^\circ$ is 1.01, supporting the accuracy of our radiometric calibration because the passive and active measurements are almost completely independent.

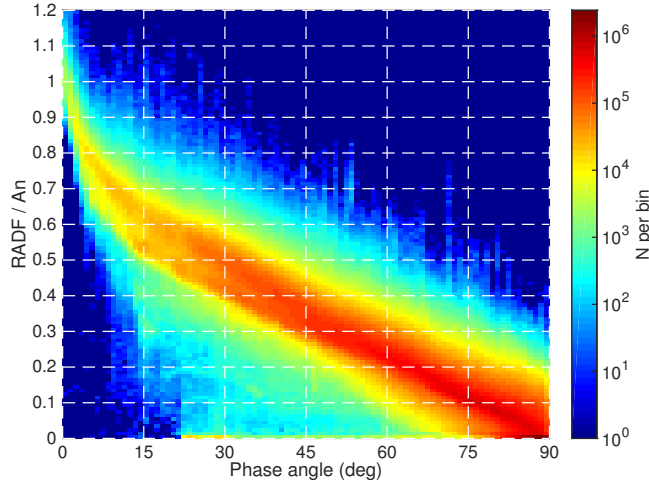


Figure 10: Photometric function (Equation 4) including all observed incidence and emission angle variation. The bin size is $1^\circ \times 0.01$.

370 5. Phase Function

The photometric function can be separated into a limb-darkening function, which contains all of the (i, e) -dependence, and a phase function, which contains all the g -dependence:

$$f(i, e, g) = D(i, e)\Phi(g). \quad (5)$$

An analytically simple limb-darkening function is the Lommel-Seeliger law,

$$LS(i, e) = \cos(i) / (\cos(i) + \cos(e)). \quad (6)$$

This law has been derived from radiative transfer theory and shown empirically to provide a reasonable first-order correction for low-albedo planetary bodies like the Moon (Hapke, 1963; Hapke et al., 2012). Therefore, we use $LS(i, e)$ and the LOLA 128 ppd global DEM to correct for the topography-dependent viewing/illumination geometry. Using other, more sophisticated, limb-darkening functions that include a phase angle dependence (McEwen, 1996; Shkuratov et al., 1999) does not affect our conclusions. Therefore, we calculate the phase function as

$$\Phi(g) = RADF(i, e, g) / A_n / LS(i, e). \quad (7)$$

To examine the different photometric behavior of the highlands and maria, we now classify the LOLA measurements as highlands or maria based on the geologic shapefile produced by Nelson et al. (2014). Figure 11 and Figure 12 show the resulting phase function for the highlands and maria, respectively. The scatter in the phase function increases dramatically at $g \gtrsim 70^\circ$ due to errors in the viewing/illumination angles. Also at high phase angles, surface locations observed while they were in partial or complete shadow appear as an excess

of points with abnormally low phase function values $\lesssim 0.2$. For these reasons, throughout this paper, we exclude points with $\Phi(g) < 0.2$ for all g , and we
380 also exclude points with $\Phi(g) > 1.2$ for $g > 60^\circ$. A phase function value of 0.2 corresponds roughly to a S/N of $\sim 5 - 10$ at $g = 85^\circ$ for typical geometries and typical maria and highland albedos. The highlands phase function is $\sim 10-20\%$ higher than that of the maria, possibly due to a larger contribution from backscattering, a larger OE width, or a smaller OE amplitude (normalizing the
385 curve at $g = 0^\circ$ causes it to shift upwards with decreasing OE amplitude). All three of these possibilities would be consistent with the phase function behavior at UV-VIS wavelengths observed with LROC (Sato et al., 2014).

Several phase functions from the literature are also overplotted in Figure 11 and Figure 12 for the case of $i = g$ and $e = 0^\circ$, which approximates the ge-
390 ometries for the majority of LOLA observations. The functions are normalized at $g = 30^\circ$ for the maria and highlands separately. Inspection of Figure 11 shows that the Clementine 950 nm highlands phase function (dashed black line; Shkuratov et al., 1999) differs little from the LROC WAC 689 nm highlands phase function (solid white line; Sato et al., 2014), and that, in terms of overall
395 shape, both provide the closest match to the LOLA 1064 nm highlands phase function. The similarity of the Clementine, LROC, and LOLA highlands phase functions is consistent with previous results that the OE angular width has little wavelength dependence for the highlands (Hapke et al., 2012; Sato et al., 2014). The SP 1068 nm highlands phase function (solid green line; Yokota et al., 2011)
400 underestimates the OE, but Yokota et al. (2011) excluded $g < 5^\circ$ when deriving their function, which also underpredicts SP data at small phase angles at other wavelengths, (see their Figure 7). The Clementine, LROC, and SP functions are very similar for $g > 30^\circ$, but they tend to underpredict the LOLA data for $g > 50^\circ$ by up to $\sim 10\%$ at $g = 85^\circ$. The shape of the Chandrayaan-1 M³
405 1070 nm highlands phase function (dashed blue line; Besse et al., 2013b) does not match the LOLA data or the other functions, perhaps due to M³ instrumental calibration uncertainties and the fact that Besse et al. (2013b) used an empirical 4th-order polynomial for the phase function whereas the others used theoretically-based models. For the maria phase function, in Figure 12, the SP
410 1068 nm model provides a better match to the LOLA data than the LROC WAC 689 nm model, perhaps because of the different wavelengths. Both of them are very similar for $g > 30^\circ$, but they underpredict the LOLA data by up to $\sim 10\%$ at $g = 85^\circ$.

6. Geologic Influences on the Phase Function

415 Now we explore how the phase function changes with various geologically important surface characteristics. The most apparent of these characteristics is albedo, with the highlands normal albedo distribution peaked at $A_n \approx 0.30$ and the maria distribution peaked at $A_n \approx 0.18$ (Lucey et al., 2014). The effect of A_n on the phase function is shown in Figure 13. Only the ~ 120 million LOLA
420 measurements at latitudes within $\pm 60^\circ$ are included to minimize the effects of topographic shading. As described previously, we exclude phase function values

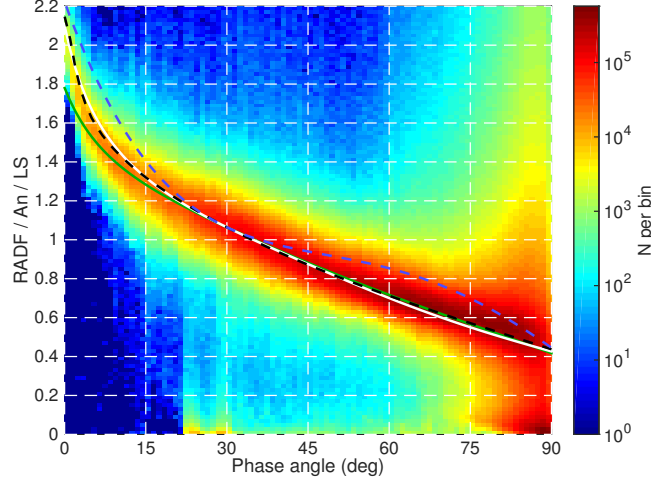


Figure 11: LOLA 1064-nm highlands phase function. Several phase functions for the highlands taken from the literature are overplotted and normalized at $g = 30^\circ$. These are: Clementine 950-nm (dashed black line; Shkuratov et al., 1999), LROC WAC 689-nm (solid white line; Sato et al., 2014), SP 1068 nm (solid green line; Yokota et al., 2011), and Chandrayaan-1 M³ 1070 nm (dashed blue line; Besse et al., 2013b).

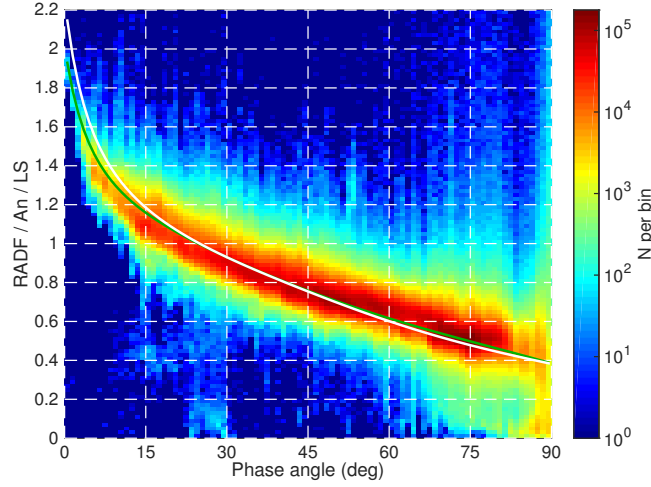


Figure 12: LOLA 1064-nm maria phase function. Two phase functions for the maria taken from the literature are overplotted and normalized at $g = 30^\circ$. These are the LROC WAC 689-nm (solid white line; Sato et al., 2014) and SP 1068 nm (solid green line; Yokota et al., 2011).

$\Phi(g) < 0.2$ for all g , and we also exclude $\Phi(g) > 1.2$ for $g > 60^\circ$. The phase function curves are calculated as the median data value within each 1° phase bin.

425 The typical spread in data values around each curve is $\sim 0.1 - 0.2$ and, more importantly for the curve-to-curve comparison, the standard error of the median is $\sim 0.001 - 0.01$ (the same is true for subsequent figures in this section). As A_n increases from 0.1 to 0.5, the phase function shifts upward by an amount that depends on phase with a maximum shift of ~ 0.3 at $g = 15 - 30^\circ$. At 430 $g = 85 - 90^\circ$, the phase function changes by < 0.1 . The slope of the phase function becomes shallower at $g \lesssim 15^\circ$ whereas the slope at $g > 30^\circ$ becomes steeper with increasing A_n . Figure 13 shows that the dichotomy in photometric behavior between the highlands and maria actually forms a continuous function of normal albedo. However, normal albedo may not be the most fundamental 435 parameter governing this behavior. Mineralogical composition, in particular the abundance of Fe and Ti, as well as the amount of time exposed to space weathering (exposure age), are other important geologic characteristics affecting albedo.

To investigate these other characteristics, we use the method of Lucey et al. 440 (2000a,b) to derive maps of FeO, TiO₂, and optical maturity (OMAT) from the Clementine multispectral reflectance maps provided by the U.S. Geological Survey at 200 meters per pixel (Eliason E., 1999; Hare et al., 2008). As before, we restrict the analysis to latitudes equatorward of 60° to reduce the effects of topographic shading in the Clementine reflectance maps, whose photometric 445 normalization assumes a flat surface on scales larger than the pixel. The LOLA measurement locations are interpolated on these maps to estimate their composition and optical maturity. The resulting FeO distribution is bimodal with peaks for the highlands and maria occurring at $\sim 5\%$ and $\sim 17\%$, respectively. The overall TiO₂ distribution is strongly peaked at $\sim 0.5\%$, corresponding to 450 typical highlands values, with a long tail toward higher values for the maria. The OMAT distribution peaks at ~ 0.17 , corresponding to typical mature regions, with a tail toward higher values representing immature regions.

The FeO abundance has a nearly identical effect on the phase function as normal albedo (Figure 14), as might be expected given the strong influence 455 of Fe²⁺ on the near-IR spectrum of silicate minerals (Burns, 1993). However, although the FeO abundance is correlated with albedo, the downward shift of the phase function with increasing FeO and decreasing A_n is not primarily an albedo effect. Theoretically, this can be understood from the fact that dividing *RADF* by A_n removes most of its dependence on singly-scattered light leaving 460 a relatively small contribution from multiple scattering. Indeed, plotting the phase function while varying FeO and restricting A_n to a small range does not significantly change the behavior shown in Figure 14. Instead, this behavior is likely due to other parameters that are correlated with composition besides single-scattering albedo, such as the relative strength of backward and forward 465 scattering in the single particle phase function, the OE amplitude, and the OE angular width (Sato et al., 2014). This is explored further in Section 7 where we model the phase function of the highlands and maria separately.

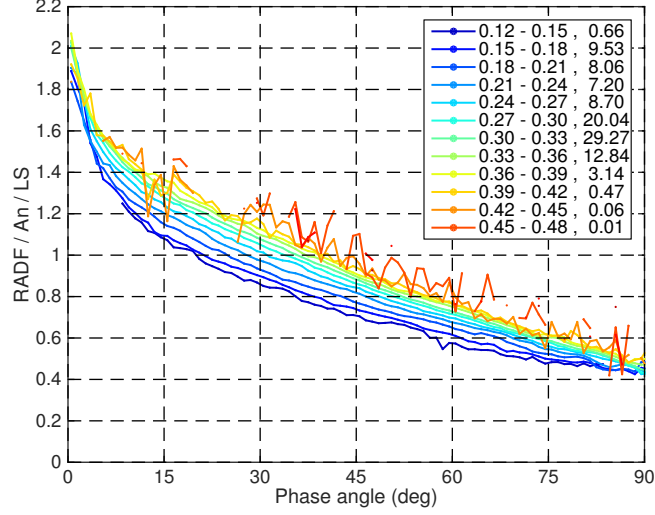


Figure 13: The effect of A_n on the LOLA 1064-nm global phase function. The curves are color-coded by A_n with warmer colors signifying larger values. The total number of data points included is ~ 120 million. The numbers after the commas in the legend give the percentage of data in each A_n bin.

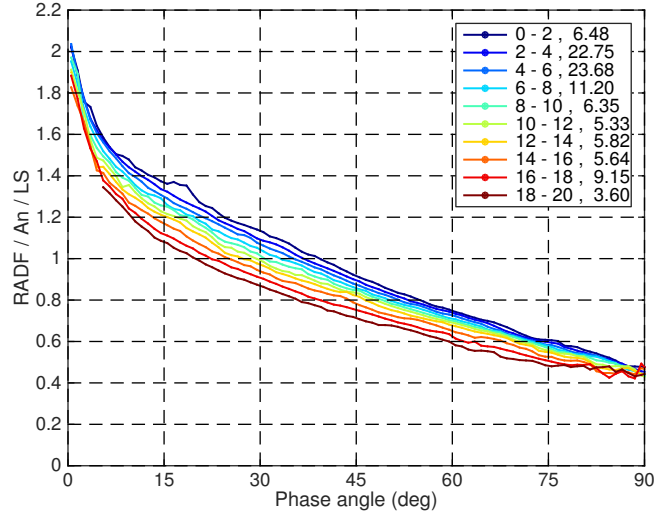


Figure 14: The effect of FeO on the LOLA 1064-nm global phase function. The curves are color-coded by FeO wt. % with warmer colors signifying larger values. The total number of data points included is ~ 120 million. The numbers after the commas in the legend give the percentage of data in each FeO bin.

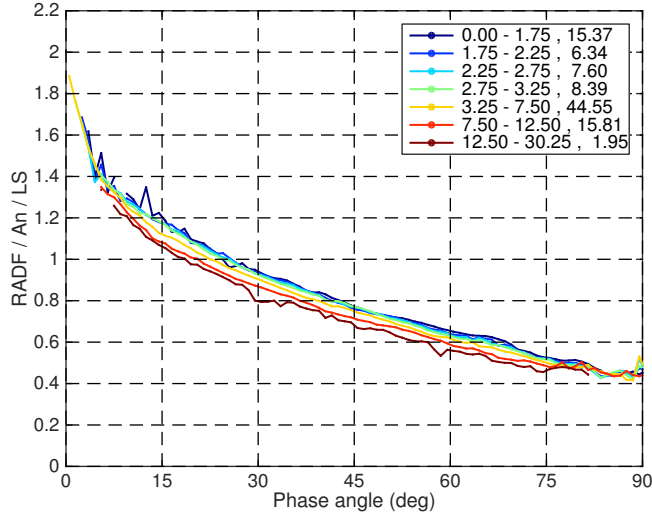


Figure 15: The effect of TiO_2 on the maria phase function ($\text{FeO} > 14\%$). The curves are color-coded by TiO_2 wt. % with warmer colors signifying larger values. The total number of data points included is ~ 20 million. The numbers after the commas in the legend give the percentage of data in each TiO_2 bin.

Variations in TiO_2 have a much smaller effect on the phase function than FeO . Over the full range of observed TiO_2 , the maria phase function shifts downward by at most ~ 0.1 (Figure 15). The highlands phase function shows no discernible trend with TiO_2 .

Figure 16 shows the effect of optical maturity on the phase function for the highlands (left panel) and maria (right panel). At a phase angle $g = 45^\circ$, the highlands phase function increases by ~ 0.25 going from the lowest OMAT bin to the highest. There is a similar, but smaller, trend for the maria phase function, which increases by ~ 0.1 at $g = 45^\circ$ going from the lowest to the highest OMAT bins. The OMAT parameter has a qualitatively similar effect on the phase function as normal albedo and FeO , as might be expected given the strong influence of the space weathering by-product, SMFe , on the spectral properties of lunar regolith (Hapke, 2001). Since OMAT is correlated with albedo, how much of the OMAT dependence is due to albedo? The answer is apparently little, for restricting A_n to a small range near either of the peaks of its bimodal distribution had little effect on the trends in this figure. Also, plotting the phase function while varying A_n and restricting FeO and OMAT to a small range showed relatively little dependence on normal albedo. Again, from a theoretical standpoint, this is due to the normalization of RADF by A_n , so other parameters that are correlated with exposure age besides albedo are likely responsible, such as the details of the single particle phase function, and OE characteristics.

We also find that the slope of the local terrain affects the phase function

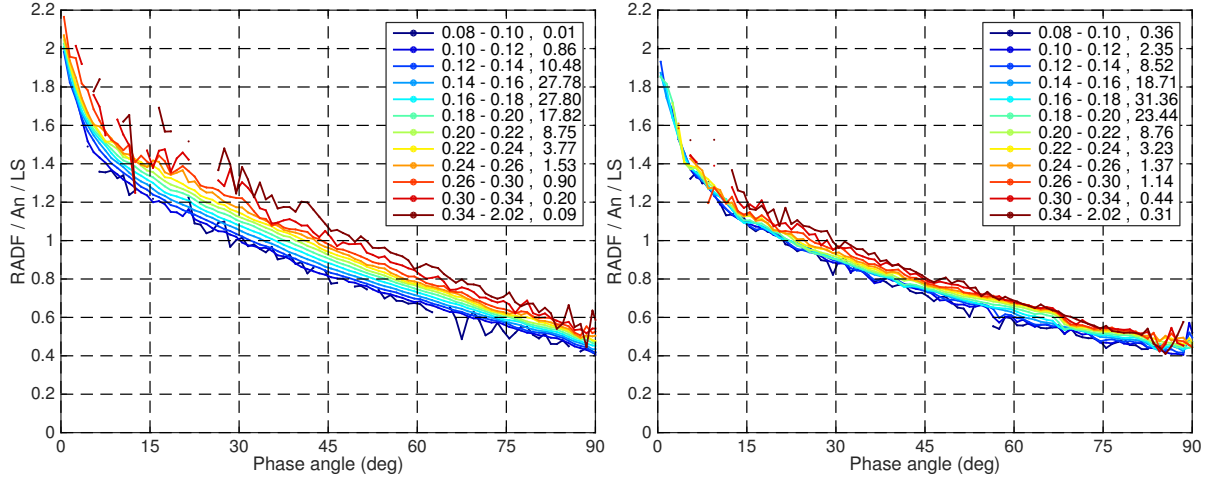


Figure 16: The effect of optical maturity on the highlands ($\text{FeO} < 8\%$; left panel) and maria ($\text{FeO} > 14\%$; right panel) phase function. The curves are color-coded by OMAT with warmer colors signifying higher OMAT values, or more immature soil. The total number of data points included is ~ 80 million (highlands) ~ 20 million (maria). The numbers after the commas in the legend give the percentage of data in each OMAT bin.

(Figure 17). Slopes $\gtrsim 20^\circ$ exhibit progressively larger upward shifts of the phase function with increasing slope, which we interpret as a result of mass wasting exposing optically immature material or reduced space weathering due to lower sky visibility. Slopes near or above the angle of repose have a similar phase function as that of the most immature material in Figure 16.

The thermal properties of the regolith are related to its physical structure, with rougher surfaces expected to have higher thermal inertia and to cool at a slower rate throughout the lunar night. Bandfield et al. (2011) exploited this behavior to derive rock abundance and nighttime soil temperature maps at 32 ppd within latitudes $\pm 60^\circ$ from thermal IR data collected by the Diviner Lunar Radiometer onboard LRO. Higher soil temperatures shift the highlands phase function to progressively higher values (Figure 18). The maria phase function has a qualitatively similar behavior, but the magnitude of the shift is reduced. We find the rock abundance and LOLA single-shot roughness (Neumann et al., 2015) to have a similar effect as the soil temperature. The rock abundance is most sensitive to rock sizes ~ 1 m and the LOLA roughness is sensitive to slope variations on scales from the footprint size (~ 50 m) down to the instrument timing resolution (~ 10 cm).

The similarity of these three quantities' influence on the phase function probably results from the fact that they are all sensitive to roughness on similar or overlapping scales. Bandfield et al. (2011) note that the soil temperature and rock abundance are highly correlated within local regions, such as inside and around craters. Possible reasons for this correlation include radiative heating from exposed rocks, the presence of small rocks that stay warmer than the

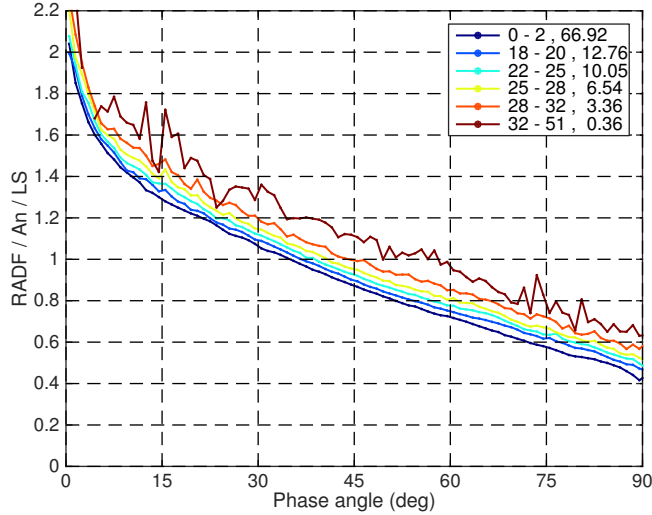


Figure 17: Highlands phase function binned according to local slope (~ 300 m baseline). The numbers after the commas in the legend give the percentage of all ~ 80 million data points in each slope bin.

regolith but are too small ($\lesssim 1$ m) to contribute to the measured rock abundance, and buried rocks that warm the surrounding regolith. When OMAT is restricted to the peak of its distribution, the phase function depends relatively little on nighttime soil temperature, rock abundance, or LOLA roughness. This highlights the correlation of these other parameters with optical maturity, and suggests that, more generally, exposure age is the dominant controlling parameter of the phase function besides Fe abundance.

One final issue to consider is the difference in resolution between the $RADF$ and A_n measurements. It is possible that localized enhancements in albedo that are resolved by the passive radiometry could be smoothed over in the 4 ppd normal albedo map causing their A_n values to be underestimated and artificially exaggerating the phase function trends found here. We examined this possibility by reprocessing the passive radiometry with a 140-shot (~ 8 km) along-track moving average and downsampling the Clementine maps and LOLA DEM to 4 ppd. The resulting phase functions and their trends with geologic parameters were not significantly changed. Because of the coarser sampling, there were not enough data points with high slopes to check the slope trend in Figure 17. However, we checked this trend by returning to the original full-resolution maps, and using FeO and OMAT together as a proxy for normal albedo to select data points whose A_n values were in the low-end tail of the highlands distribution, and, therefore, less likely to have been underestimated by the large pixel size of the A_n map. Choosing points in this way left the slope trend unchanged for slopes $< 32^\circ$, but there were not enough points with higher slopes to check the largest slope bin. Therefore, it seems unlikely that the resolution mismatch

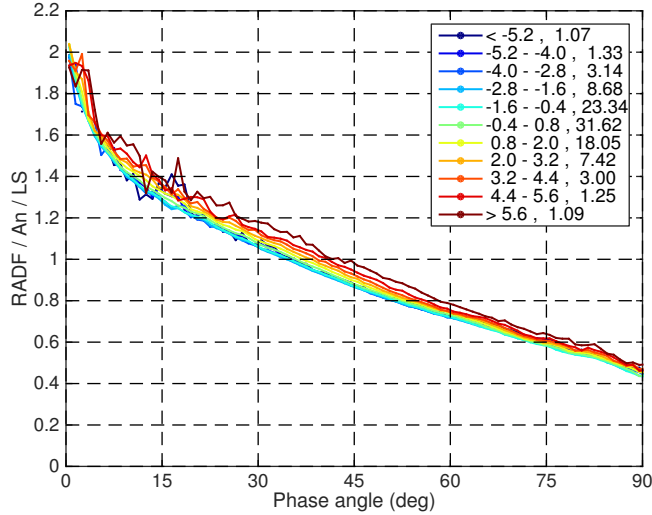


Figure 18: Highlands phase function binned according to Diviner nighttime soil temperature. Temperatures are expressed as °C deviation from the latitudinal average. The numbers after the commas in the legend give the percentage of all ~ 80 million data points in each temperature bin.

between the $RADF$ and A_n measurements has strongly impacted the phase
 540 function behavior in this section.

7. Hapke Function Modeling

7.1. Model Details

In this section, we model the observations to learn more about the physical
 properties of the regolith. We adopt the isotropic multiple scattering approxi-
 545 mation of Hapke (2012b) which describes the $RADF$ with the equation,

$$RADF(i, e, g) = LS(i_e, e_e) K \frac{w}{4} \frac{[p(g)(1 + B_{S0}B_S(g)) + M(i_e, e_e)]}{[1 + B_{C0}B_C(g)]S(i, e, \psi)} \quad (8)$$

This equation contains 9 free parameters theoretically related to the light
 scattering properties of the regolith particles, the particle size distribution,
 porosity, and sub-pixel roughness. For a detailed explanation of this equation,
 we refer the reader to Hapke (2012b) and references therein. In application,
 550 we follow closely the method used by Sato et al. (2014) with the notable ex-
 ception that we make use of the actively-derived 1064-nm normal albedo, A_n ,
 to reduce the number of free parameters and avoid having to divide the data
 into separate albedo groups as in Yokota et al. (2011). The data to be fitted
 consist of the median photometric function (Equation 4) in 1° -cubed voxels

555 in (i, e, g) . Voxels with $i > 75^\circ$, $e > 30^\circ$, or $g > 97^\circ$ are excluded. From Equation 4 and the definition of A_n , the model photometric function is calculated as $RADF(i, e, g)/RADF(e, e, 0)$ evaluated at each voxel’s central values of (i, e, g) . Voxels with $RADF/A_n < 0.02$ are excluded as they are contaminated by shadows and errors in the derived photometric angles at high phase. This
 560 cut corresponds roughly to a S/N of $\sim 5 - 10$ for typical maria and highland albedos.

The LS factor in Equation 8 is the Lommel-Seeliger Law with the “effective” incidence and emission angles, i_e and e_e , to account for roughness with the parameter, $\overline{\theta_p}$ (Hapke, 2012b). This parameter describes the mean slope of
 565 the surface on scales relevant to the wavelength and pixel size. In a 6° -wide strip around the whole equator, Sato et al. (2014) derived a mean value of $\overline{\theta_p} = 23.4^\circ$ at UV-VIS wavelengths with little dependence on wavelength or geologic context. We adopt this value throughout our analysis.

The parameter, K , is a function of the filling factor, ϕ , in the optically
 570 relevant portion of the lunar regolith (the upper ~ 1 mm). Recent analyses suggest $\phi \approx 0.2$ (Ohtake et al., 2010; Hapke and Sato, 2015), corresponding to a porosity, $P = 1 - \phi = 0.8$ and $K \approx 1.3$. However, to keep our results more directly comparable to those of Sato et al. (2014), we set $\phi = 0$, resulting in $K = 1.0$. This should not affect our results, however, because the multiplicative
 575 factor of K in Equation 8 cancels out in the photometric function, leaving only a small contribution from an additional factor of K that appears in the multiple scattering term, $M(i_e, e_e)$. Porosity may still affect the model through its influence on other model parameters, such as the angular width of the shadow hiding OE (SHOE), h_S (Hapke, 2012b; Déau et al., 2013).

The single-particle phase function, $p(g)$, is a double-lobed Henyey-Greenstein (HG) function with two parameters, the shape parameter, b , and asymmetry parameter, c . The latter is set by b through the empirical “hockey-stick” relation

$$c = 3.29 \exp(-17.4b^2) - 0.908, \quad (9)$$

580 which was derived by (Hapke, 2012a) from a meta-analysis of various laboratory sample measurements.

The amplitudes of the SHOE and coherent backscatter OE (CBOE) are set by the parameters, B_{S0} and B_{C0} , respectively. To be consistent with Sato et al. (2014), we ignore the CBOE by setting $B_{C0} = 0$. The CBOE and SHOE are very difficult to disentangle without polarization measurements (Hapke, 2012b). Ignoring the CBOE can lead to derived values of $B_{S0} > 1$ if coherent backscatter is present. Rather than being a free parameter, the amplitude of the SHOE is determined by rearranging Equation 8 into the form

$$B_{S0} = \frac{8A_n - wM(e_e, e_e)}{wp(0)} - 1, \quad (10)$$

given w , b , and A_n , a representative normal albedo for the sample being fitted. In practice, we use the mode of the sample’s A_n distribution.

That leaves three free parameters: the single-scattering albedo, w , the HG
 585 shape parameter, b , and the angular width of the SHOE, h_S . We solve for the

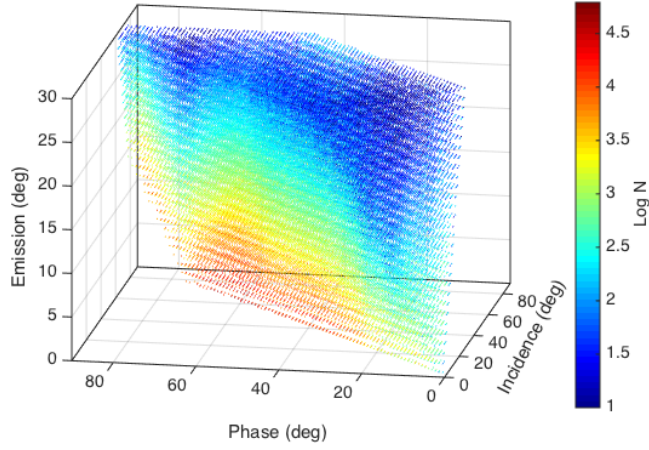


Figure 19: 3-D scatter plot color-coded by the number of data points within the $\sim 63,000$ voxels for the total highlands sub-sample. The total number of data points summed over all voxels is ~ 60 million.

best-fit combination of parameters by minimizing the weighted sum of squared errors over all N voxels,

$$SSE = \sum_{i=1}^N \rho_i r_i^2 = \sum_{i=1}^N \rho_i \left(n_i \frac{d_i - m_i}{m_i} \right)^2, \quad (11)$$

where n_i is the number of observations in voxel i , d_i and m_i are the data and model values for voxel i calculated as explained previously, and ρ_i is the voxel's weight. To downweight data outliers and imperfections in the model, we use the weighting function $\rho_i = \min(2.25\sigma^2/r_i^2, 1.0)$ where σ is the standard deviation of all voxel errors. Since most of the observations are taken at near-nadir viewing geometry, voxels with $e \approx 0$ and $i \approx g$ tend to receive the most weight in the fit. We employ a downhill simplex minimization algorithm (Lagarias, 1998), initialized to 30 different random starting locations, to find the best-fit parameters.

As LOLA collects more data, the phase coverage at each surface location will broaden, eventually enabling a spatially-resolved map of model parameters. In the present study, we take the approach of splitting up the data into global geologic units and fitting each one separately. First, we separate the maria and highlands based on FeO, and then we divide each of these two terrains into optically mature and immature sub-samples based on OMAT. We also divide the maria into low and high TiO₂ sub-samples. As before, we restrict the analysis to latitudes within $\pm 60^\circ$ to limit topographic shadowing effects.

7.2. Model results

The best-fit model parameters are listed in Table 4. The parameter errors represent the standard deviation of 200 bootstrap resamplings of the data (with

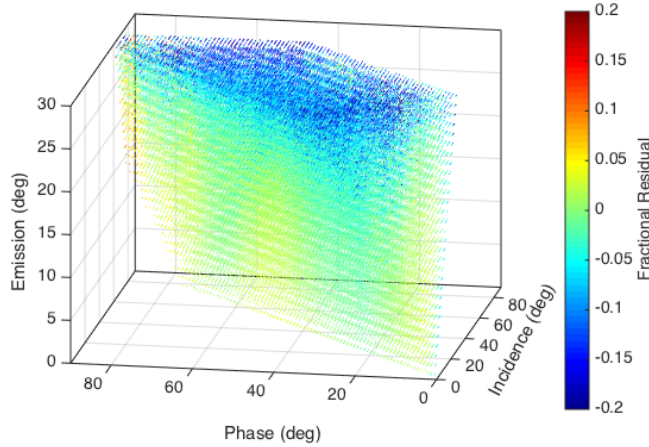


Figure 20: Fractional residuals of best-fit Hapke model for total highlands sub-sample. Voxels are color-coded by fractional residual defined as $(\text{model} - \text{data})/\text{model}$.

replacement) following the same fitting procedure.

Figure 19 shows the number of data points within each voxel for the total highlands sub-sample. The magnitude of fractional residuals of the best-fit model (Figure 20) are $< 5\%$ for most geometries, but tend to increase with emission angle, or local slope. Figure 21 compares the data and best-fit model values for all voxels as a function of phase angle for all incidence and emission angles. The model tends to underestimate the data at high emission angles, and this is manifested in Figure 21 as an excess of blue (data) points above the red (model) points, most notably for $g < 60^\circ$. Conversely, the envelope of model voxels with $e < 10^\circ$ matches well that of the data. The mismatch at high- e could be due to a deficiency in the Hapke model at predicting the reflectance at high emission angle. On the other hand, Figure 17 shows that surfaces with high slopes, on average, have a different phase function than flat surfaces, probably because of their relative immaturity. The low-OMAT (mature) highlands subsample still had an excess of data voxels above the model although it was not as significant. The OMAT parameter assumes a flat surface on scales larger than the pixel (Lucey et al., 2000a), so it is possible that, by virtue of their high slopes, these voxels' OMAT values are underestimated causing them to be erroneously included in the mature subsample. Finally, we note that, at low phase angles, the model OE is too wide, but this is unlikely due to the high- e data skewing the fit because excluding $e > 10^\circ$ from the fit actually resulted in a $\sim 10\%$ larger value of h_S .

As expected, the model results indicate that the highlands have a higher single scattering albedo, w , than the maria. This is, at least partially, due to our use of Equation 10, which couples the parameters, B_{S0} , w , b , and A_n . Setting A_n to a 10% higher value would have a similar effect on w . The highlands have a lower value of b compared to the maria, and because c is coupled to

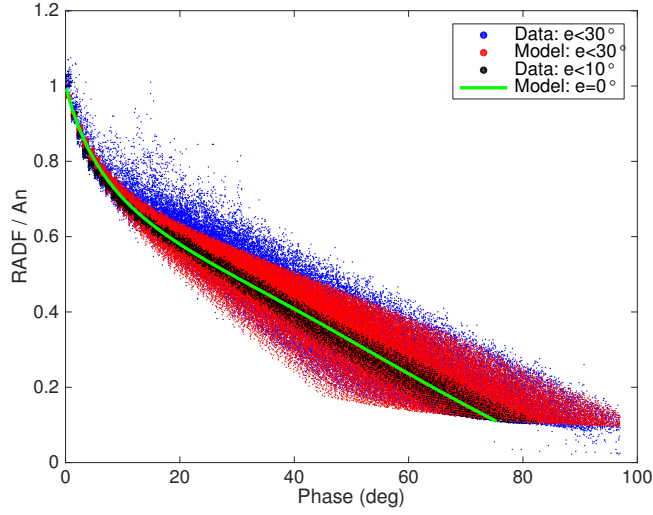


Figure 21: Comparison of highlands data ($\text{FeO} < 8\%$) and best-fit Hapke model. In the order in which they are plotted, the blue points show the data for $e < 30^\circ$, the red points correspond to the model for $e < 30^\circ$, the black points are the data for $e < 10^\circ$, and the green line represents the model for $e = 0$ and $i = g$. The faint cut-off at $\text{RADF}/A_n \sim 0.1$ is due to the 75° limit imposed on incidence angle. For plotting clarity, a small random offset $< 0.5^\circ$ is added to the phase angles.

635 b through Equation 9, c is higher for the highlands than for the maria. This means that the highlands have a higher backscattering fraction than the maria, a result in qualitative agreement with Sato et al. (2014). However, our derived value of $b = 0.167 \pm 0.004$ is significantly lower than those derived by Sato et al. (2014), who found $b = 0.23 - 0.24$ for the highlands with little dependence on
640 wavelength. The cause of this difference is presently unclear, but it could be related to uncertainties in the LOLA or SP radiance calibration.

In addition, we find that the total highlands sub-sample has a higher OE amplitude, B_{S0} , than the maria. Our best-fit value for the highlands, $B_{S0} = 1.60 \pm 0.03$, matches that derived by Sato et al. (2014) for the highlands at 689
645 nm and is consistent with the flattening they observed in the trend of decreasing B_{S0} with increasing wavelength. Our best-fit value of $B_{S0} = 1.50 \pm 0.02$ for the maria is lower than their value of 1.88 at 689 nm, implying that, in contrast to the highlands, the wavelength trend for the maria does not flatten out moving toward the near-IR. Finally, we find that, compared to the maria, the highlands
650 have a larger angular width of the OE, h_S , which is consistent with Sato et al. (2014). Our best-fit value of h_S for the total highlands sample is slightly higher than the values found by them at all wavelengths ($0.075 - 0.08$), yet within their error bars, but as noted previously the OE width of the best-fit model is slightly overestimated for $e < 10^\circ$. Our best-fit value of 0.042 ± 0.001 for the total maria
655 sample is lower than their value of 0.05, but consistent with their error bars,

Table 4: Best-fit Hapke parameters for different geologic sub-units¹.

| Group | w | b | c | B_{S0} | h_S | A_n |
|--------------------------|-------------------|-------------------|-----------------|-----------------|-------------------|-----------------|
| Highlands: FeO < 8% | | | | | | |
| Total | 0.486 ± 0.004 | 0.167 ± 0.004 | 1.12 ± 0.04 | 1.60 ± 0.03 | 0.083 ± 0.002 | 0.30 ± 0.01 |
| OMAT < 0.14 | 0.465 ± 0.005 | 0.199 ± 0.007 | 0.74 ± 0.08 | 1.62 ± 0.01 | 0.069 ± 0.001 | 0.28 ± 0.01 |
| OMAT > 0.24 | 0.544 ± 0.008 | 0.17 ± 0.01 | 1.1 ± 0.2 | 1.75 ± 0.06 | 0.140 ± 0.005 | 0.36 ± 0.01 |
| Maria: FeO > 14% | | | | | | |
| Total | 0.356 ± 0.008 | 0.266 ± 0.009 | 0.05 ± 0.08 | 1.50 ± 0.02 | 0.042 ± 0.001 | 0.18 ± 0.01 |
| OMAT < 0.14 | 0.30 ± 0.01 | 0.22 ± 0.02 | 0.5 ± 0.2 | 1.66 ± 0.04 | 0.046 ± 0.003 | 0.18 ± 0.01 |
| OMAT > 0.24 | 0.36 ± 0.02 | 0.20 ± 0.04 | 0.7 ± 0.5 | 1.5 ± 0.1 | 0.051 ± 0.005 | 0.20 ± 0.01 |
| TiO ₂ < 3.00% | 0.388 ± 0.006 | 0.269 ± 0.007 | 0.03 ± 0.06 | 1.55 ± 0.02 | 0.048 ± 0.002 | 0.20 ± 0.01 |
| TiO ₂ > 9.75% | 0.278 ± 0.009 | 0.26 ± 0.01 | 0.1 ± 0.1 | 1.86 ± 0.02 | 0.048 ± 0.001 | 0.16 ± 0.01 |

¹ $K = 1$ and $\overline{\theta_p} = 23.4^\circ$ in all cases. The asymmetry parameter, c , was determined by Equation 9 given b . The amplitude of the SHOE, B_{S0} , was determined by Equation 10. A_n is the observed mode for each subsample and the error of A_n is the histogram bin width.

suggesting the marginally decreasing wavelength trend they observed continues to the near-IR. Like Sato et al. (2014), we find that the parameters, h_S , b , and c , do not significantly vary with optical maturity or Ti abundance in the maria.

Compared to optically mature highlands, optically immature highlands have a higher single scattering albedo, w , a lower phase function shape parameter, b , a higher backscatter fraction, c , a larger OE amplitude, B_{S0} , and a larger OE angular width, h_S . These results are qualitatively in line with what we might expect from the analysis in Section 6. With the exception of the OE amplitude, these results are also consistent with the trends observed by Sato et al. (2014) for optically immature highlands versus mature highlands. They used a different relation from Equation 10 to set B_{S0} in the UV-VIS wavelength range, which may be responsible for the different behavior we observe for B_{S0} in the mature vs. immature highlands.

8. Discussion

8.1. Geologic influences on the global phase function

In summary, the 1064-nm phase function shows various levels of dependence on several geologic properties. Of the properties explored here, we found that FeO and OMAT have the most control over the phase function. Globally, they act in the opposite sense; as FeO increases, the near-IR phase function shifts downwards, and as OMAT increases (i.e., as the surface becomes more optically immature), the phase function shifts upwards. This is not primarily an albedo effect, but is instead likely due to other parameters controlling the reflectance,

such as the single particle phase function and OE characteristics, which themselves may be correlated with albedo and more fundamental soil properties like composition, porosity, and grain size distribution. Although the albedo does generally decrease with increasing FeO and decreasing OMAT, our use of the LOLA 1064 nm normal albedo allows us to separate out most of the explicit albedo-dependence in the reflectance and study these other controlling parameters.

We also found that regolith thermal inertia, quantified by Diviner nighttime soil temperature, and roughness on decimeter to decameter scales, measured by Diviner rock abundance and LOLA footprint-scale topography, have qualitatively similar, but quantitatively smaller effects on the phase function compared to optical maturity. However, when OMAT is held fixed, the phase function shows relatively little dependence on these other thermophysical properties. We interpret this to mean that, on a global scale, exposure age, and all of its associated effects on soil/grain properties, is the dominant controlling parameter besides FeO abundance. Recently, Hemingway et al. (2015) presented evidence for latitudinal spectral variations in the maria, attributed to reduced solar wind flux at high latitudes. In future work, we will examine any possible variations in the phase function associated with such latitude-dependent space weathering.

The highlands phase function also depends on local slope (at ~ 300 m baselines) for slopes $\gtrsim 20^\circ$. On these high slopes, the phase function behaves more optically immature with increasing slope. We interpret this as a sign of mass wasting exposing fresh material and/or reduced space weathering due to lower sky visibility. Whatever the cause, this behavior has implications for stereophotoclinometry terrain models, which must assume a phase function to reconstruct topography from albedo variations. These models should account for changes in the phase function of highly sloped surfaces to have the most accurate results.

8.2. Phase difference map

Although the phase coverage of the current dataset is not dense enough to derive a spatially resolved Hapke parameter map as in Sato et al. (2014), it is still possible to identify spatially localized deviations from the globally typical phase function, which may be caused by real geologic variations. With this in mind, we made a color composite “phase difference” map in the bottom panel of Figure 22. This map shows the median residual between every measurement and the global phase function for that point’s phase and FeO bilinearly interpolated on the phase function grid of Figure 14 to facilitate comparison between the maria and highlands. Thus, for every LOLA measurement, the phase difference is defined as

$$\Delta\Phi(g) = \Phi(g) - \langle\Phi(g, \text{FeO})\rangle, \quad (12)$$

where $\langle\Phi(g, \text{FeO})\rangle$ is the interpolated grid value. The red, green, and blue channels of the phase difference map show the median $\Delta\Phi(g)$ within the phase

720 ranges $60 - 90^\circ$, $30 - 60^\circ$, and $0 - 30^\circ$, respectively. Points with $\Phi(g) < 0.2$ are excluded for all g , and, for $g > 60^\circ$, we also exclude points with $\Phi(g) > 1.2$.

As explained previously, FeO and OMAT have the greatest effect on the phase function. Since we have removed the major FeO variations, the brightness and color variations in the phase difference map are generally correlated with variations in the OMAT map. Indeed, many of the most immature re-
725 gions in the OMAT map are visible in the phase difference map as intensity enhancements. Above 30° N, these enhancements tend to be green or yellow because of the lack of data with $g < 30^\circ$, but this still indicates more excess power (more positive residuals) at phase angles $30 - 60^\circ$ than $60 - 90^\circ$, consistent with the behavior observed in Figure 16. Despite some data gaps due
730 to the incomplete Clementine coverage, and the lack of low-phase information at its latitude, the crater, Giordano Bruno, and its surroundings are clearly visible (A, 35.9° N 102.8° E). Its ejecta blanket shows some color variation and its ejecta rays are barely discernable as green and blue enhancements extending NW and SE from the crater. Several other young craters and their immature
735 ejecta are clearly visible in the phase difference map, most notably Copernicus (B, 9.62° N 339.92° E), whose interior and immediate surroundings appear green and yellow, and Proclus (C, 16.1° N 46.8° E) with its two bright rays extending NW and SE. Interestingly, the Aristarchus plateau does not have a significant enhancement in the phase difference map despite being one of the most promi-
740 nent features in the OMAT map (D, 23.7° N 312.6° E). Instead, the plateau's spatially localized appearance in the phase difference map is more consistent with the 1064 nm normal albedo map (Figure 9). The Aristarchus plateau is a well-known site of extensive volcanic activity with a regional dark mantle deposit thought to have a significant concentration of pyroclastic glasses (Gaddis
745 et al., 1985; Lucey et al., 1986). The OMAT parameter could be overestimated in this region because it is not calibrated for pyroclastic glass. In addition, the different grain properties of the pyroclastic material may change the phase function relative to typical regolith with the same exposure age.

8.2.1. *Jackson crater*

750 A striking large-scale feature in the phase difference map is the Copernican-aged Jackson crater (E, 22.1° N 196.7° E, diameter = 71 km), which appears as a blue-green enhancement surrounded by pink pixels with an overall SW-NE orientation. Its bright ejecta are visible as slightly purple enhancements extending out hundreds of km. This crater has a dark halo visible in the OMAT
755 map and 1064 nm normal albedo map, which is generally considered to be an impact melt deposit (McEwen et al., 1993; Belton et al., 1994; Grier et al., 2001; Hirata et al., 2010). The dark halo has a spectral signature distinct from the surrounding ejecta as seen in the Clementine UV-VIS color-ratio composite image (top panel of Figure 23). The pink pixels surrounding the crater in the
760 phase difference map (bottom panel of Figure 23) are approximately co-spatial with the dark halo deposit. Even though the dark halo and bright rayed ejecta are likely to have the same age, the halo has lower OMAT values (mean and standard deviation of 0.20 ± 0.02 vs. 0.22 ± 0.02) because the OMAT parameter

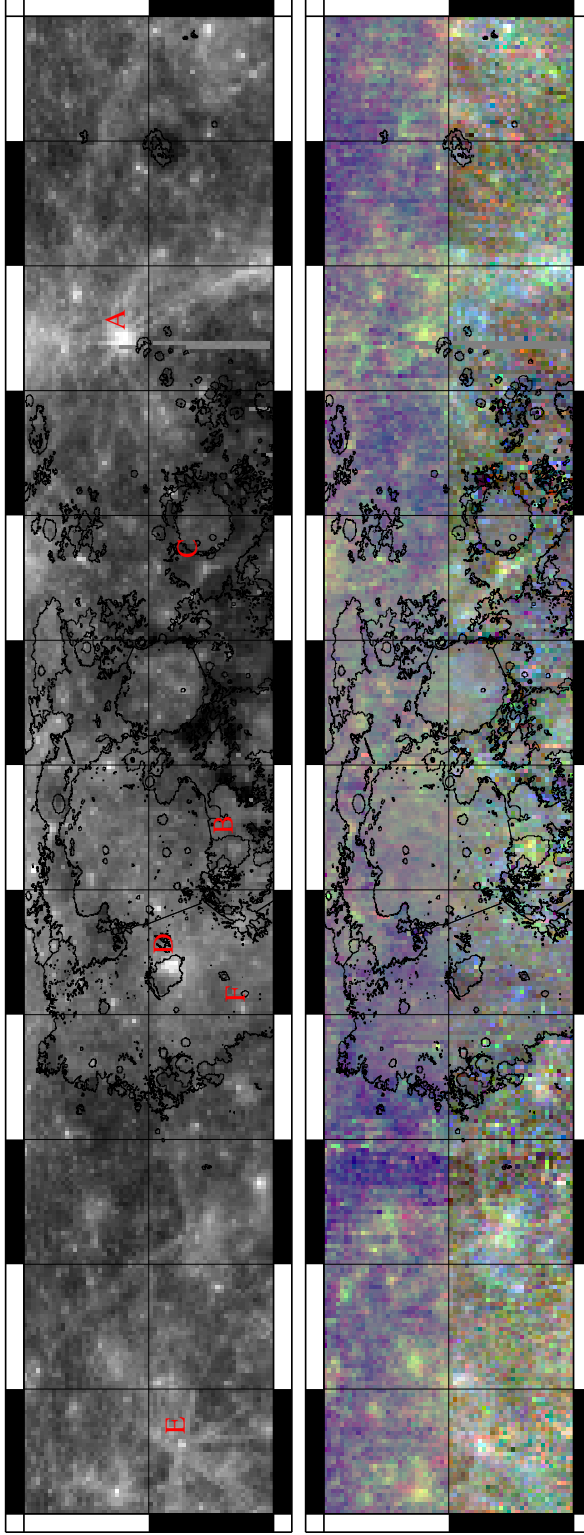


Figure 22: Top: OMAT parameter mapped at 1 ppd with a color scale that ranges from 0.1 (black) to 0.3 (white). Map covers $0 - 60^\circ$ N and is centered on 0° E. Grid lines are spaced every 30° . The maria are outlined with the Nelson et al. (2014) shapefile. Several features discussed in the text are labeled: The craters, Giordano Bruno (A), Copernicus (B), Proclus (C), and Jackson (E); the Aristarchus plateau (D) and Reiner Gamma Formation (F). Bottom: Color composite phase difference map showing the median difference from a globally representative phase function (see text for details). Different phase angle ranges control the color channels: $0 - 30^\circ$ (blue), $30 - 60^\circ$ (green), and $60 - 90^\circ$ (red). Each channel's scale is normalized to the difference range ± 0.10 in phase function units. The blue channel for latitudes above 30° N is set to a constant phase difference value of 0, causing only red and green hues there, due to the lack of data with phase $< 30^\circ$.

has a different behavior over glassy deposits compared to normal regolith (Lucey
765 et al., 2000b).

To further examine the phase function behavior of Jackson and its environs,
we selected data within four regions of interest which are drawn on the maps
in Figure 23: inside the crater, dark halo, ejecta rays, and off-ejecta. The FeO
abundances for the LOLA data in these regions are 4.6 ± 1.2 , 4.3 ± 0.8 , 3.6 ± 0.8 ,
770 and $4.0 \pm 0.9\%$, respectively. Evidently, any glassy deposit in the dark halo
contributes at most a $\sim 10 - 20\%$ error in FeO, consistent with the OMAT
parameter. Figure 24 quantifies the color variations seen in the phase difference
composite by plotting the values of the RGB color channels for all data within
each region of interest. The error bar of each point is the central 68th percentile.
775 The crater data are higher in the 15° and 45° phase bins, which explains why
the crater appears blue-green in the composite. The crater also exhibits the
most variation within each phase bin. The dark halo phase difference is highest
in the 75° phase bin, which explains its overall pink hues. The off-ejecta region,
which appears brown in the phase difference composite, has the smallest phase
780 function differences in magnitude and absolute value. Taken together, these
data indicate that most of the variation in the overall shapes of the Jackson
phase functions comes from the 75° phase bin. All else being equal, a rougher
surface will generally have reduced reflectivity by an amount that increases with
phase angle (Hapke, 1984; Shkuratov et al., 2003). One possible interpretation,
785 then, is that the surface of the dark halo is smoother than the other regions on
photometrically dominant scales ($\sim 0.1 - 1$ mm) whereas the surface within the
crater is rougher (Helfenstein and Shepard, 1999; Goguen et al., 2010). Other
regolith properties, such as porosity and grain size, may also contribute to these
phase function variations (Cord et al., 2003; Shepard and Helfenstein, 2007).

790 8.2.2. *Reiner Gamma*

Another feature of interest in the phase difference map is the Reiner Gamma
Formation (F, 7.4° N 301.5° E). Figure 25 shows a close-up of the phase differ-
ence color composite map centered on Reiner Gamma and superimposed on the
grayscale Clementine 415 nm reflectance map (200 mpp). The phase difference
795 map shows an enhancement over Reiner Gamma’s heart between $\sim 7 - 8^\circ$ N.
There are no clear enhancements associated with the SW and NE extensions,
but their relatively low albedos and smaller areal fraction within each 1° pixel
are partly responsible for their non-detection in this map. In fact, we also pro-
duced a higher-resolution grayscale phase difference map averaging all 3 phase
800 bins together, and parts of the NW extension did become visible. However, for
our present purposes, it is sufficient to focus on the heart, which is where the
strongest magnetic fields and brightest areas reside (Hood et al., 2001). We ex-
tracted the passive radiometry data within the bright lanes and central portion
of the heart, excluding the dark lanes, yielding an “on-swirl” data sample of
805 $\sim 4,600$ points. For a control sample, we used data within a 2° -wide annulus
with inner radius of 2° while excluding any overlapping areas close to the SW
and NE extensions. This “off-swirl” sample consisted of $\sim 110,000$ points. The
mean and standard deviation of FeO, TiO_2 , and OMAT for the on-swirl sample

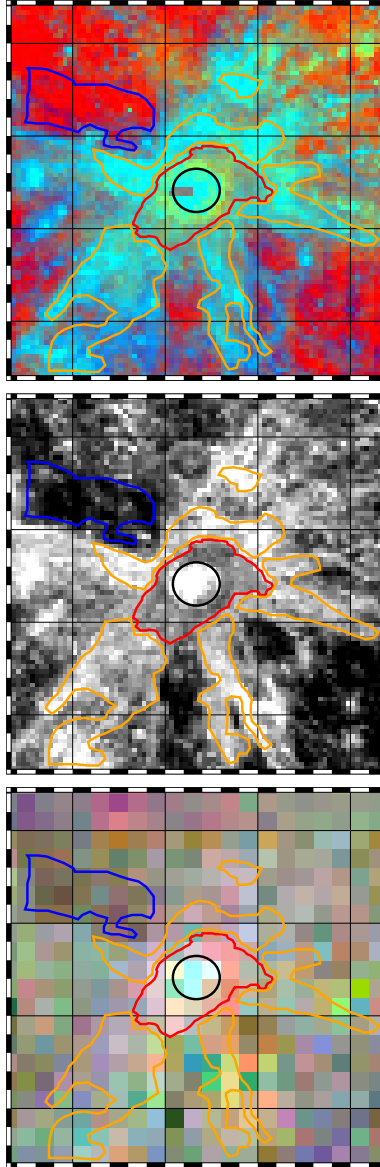


Figure 23: Spectral and photometric maps (simple cylindrical projection) centered on Jackson crater (black circle; 22.1°N 163.3°W). Grid lines are spaced 5° apart. Top: Clementine 4 ppd UV-VIS color ratio composite with spectral ratios 415/750-nm (blue), 750/950-nm (green), and 750/415-nm (red). Middle: Clementine 4 ppd 750 nm reflectance. Bottom: LOLA 1064 nm phase difference color composite. Phase difference data within the outlined regions of interest (crater, dark-halo, ejecta, and off-ejecta) are plotted in Figure 24.

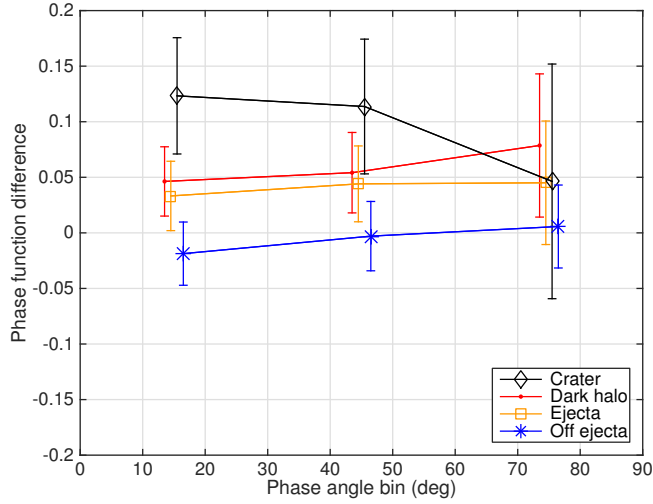


Figure 24: Phase difference data (Equation 12) within the outlined regions of interest around Jackson (crater, dark-halo, ejecta, and off-ejecta) in Figure 23. The differences are measured with respect to the global phase function for the same FeO.

are, respectively, $16.3 \pm 0.4\%$, $4.0 \pm 0.7\%$, and 0.25 ± 0.03 , while the values for the off-swirl sample are $18.6 \pm 0.4\%$, $8.2 \pm 1.5\%$, and 0.18 ± 0.02 .

We show the phase function of the on-swirl data as a 2-D histogram in Figure 26. Superimposed on the histogram are lines corresponding to the phase functions of the off-swirl sample (green), and the global dataset for the same FeO, TiO₂, and OMAT as the off- and on-swirl data (cyan and white, respectively). Because we are looking at a very small region, the phase angle sampling is drastically reduced compared to the global dataset, and the individual orbits passing through this region each sample essentially one phase angle. The off-swirl sample is predominantly optically mature mare soil and its phase function (green line) is very similar to its compositionally-equivalent global average (cyan line). The on-swirl sample shown in the histogram is systematically higher than the off-swirl sample (green line), consistent with it having a higher OMAT than its surroundings. The on-swirl sample is also displaced from its compositionally-equivalent global average (white line). However, the unusual regolith properties in the on-swirl regions may cause the Clementine spectral diagnostics, which were calibrated to returned lunar samples, to be less accurate there (Lucey et al., 2000a,b). This may be the reason why the on-swirl data have lower FeO and TiO₂ abundances than the off-swirl sample (Kramer et al., 2011; Blewett et al., 2011). Using the possibly more accurate off-swirl FeO and TiO₂ values for the on-swirl regions only enhances the offset between the on-swirl and global phase functions. This offset was only slightly reduced when using the uniformly downsampled low-resolution datasets described in Section 6. Hence, it is unlikely to be entirely an artifact of the resolution mismatch between the passive

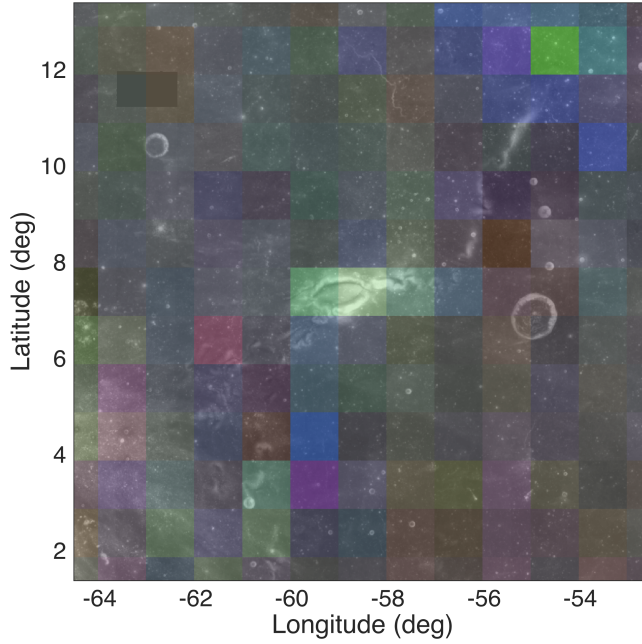


Figure 25: Close-up of phase difference map from Figure 22 centered on Reiner Gamma and superimposed on the grayscale Clementine 415 nm reflectance map.

radiometry and A_n map-interpolated measurements.

Taken at face value, these results suggest that the on-swirl phase function
 835 deviates from the global trend with OMAT observed in Figure 16, and be-
 behaves like a less optically mature soil than indicated by its OMAT. However,
 the OMAT parameter itself may also be biased in the on-swirl regions for the
 same reason as FeO and TiO₂. With manual trial-and-error, we found that the
 compositionally-equivalent global phase function could provide a much better
 840 match to the on-swirl data if it had OMAT values of $\sim 0.36 - 0.42$ instead of
 0.25. This de-coupling of the phase function and OMAT parameter could be due
 to differences between their behaviors in the presence of the atypical regolith
 properties of Reiner Gamma, which may include an altered roughness, poros-
 ity, grain size distribution, and/or non-standard mix of weathering byproducts
 845 (Hood and Schubert, 1980; Kreslavsky et al., 2000; Pinet et al., 2000; Kreslavsky
 and Shkuratov, 2003; Garrick-Bethell et al., 2011; Kramer et al., 2011). This
 highlights the fact that the phase function could potentially be a useful tool used
 in conjunction with spectral analysis for constraining models of space weather-
 ing.

8.3. Hapke modeling

850 Finally, what can we conclude from the Hapke modeling? The key results
 found by Sato et al. (2014) were that, relative to the highlands, the maria

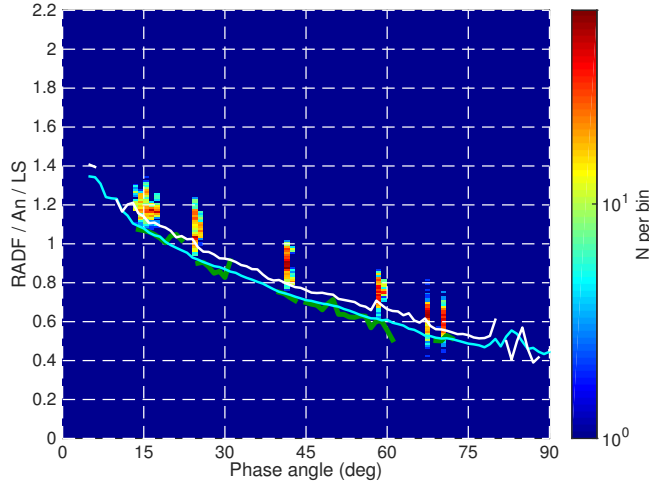


Figure 26: Phase function of Reiner Gamma’s on-swirl data shown as a 2-D histogram. The cyan and white lines correspond to the global phase functions for the same FeO, TiO₂, and OMAT as the off- and on-swirl data, respectively. The green line is the phase function for off-swirl data within a radius of 2°.

exhibited decreased backscattering (lower c , higher b), a narrower OE width (smaller h_S), and a larger OE amplitude (larger B_{S0}). Our results are consistent with the first two items, but we derived a lower OE amplitude for the maria ($B_{S0} = 1.50 \pm 0.02$) than highlands ($B_{S0} = 1.56 \pm 0.03$). Given the remaining uncertainties in the passive radiometric scale, this difference may not be significant. Taken at face value, this means that the decreasing trend of B_{S0} with wavelength that Sato et al. (2014) observed in the maria continues into the near-IR, and the flattening they observed for the highlands continues into the near-IR.

We found that the shape of the maria phase function had less dependence on the geologic parameters OMAT, rock abundance, soil temperature, and roughness compared with the highlands. This is consistent with the result of Sato et al. (2014) that the Hapke parameters h_S , b , and c are uncorrelated with geologic context within the maria. Sato et al. (2014) found that fresh craters in the maria do not exhibit higher h_S as observed in the highlands, and that maria with low and high Ti concentrations do not show a clear difference in b and c values. They attributed the h_S result to a difference in physical strength between the maria and highlands materials, and the b - c result to the fact that ilmenite lowers the albedo of backscattering agglutinates, but also decreases the fraction of forward scattering silicates, resulting in no net effect on the relative proportions of forward and backward scattering.

9. Summary and Conclusions

In this work, we have presented the initial calibration and results of passive radiometry collected by LOLA over the course of ~ 12 months during the LRO extended science mission phase 2. We characterized the time and temperature dependent dark-current, daytime temperature dependent responsivity variations, and inter-channel responsivity variations. The LOLA passive radiometry was brought onto the absolute radiance scale of the SELENE SP by matching up measurements taken with the two instruments. The resulting photometric precision was estimated to be $\sim 5\%$ with an absolute uncertainty of at most $\sim 20\%$.

We compared the resulting 1064-nm phase function to others reported in the literature, and found reasonable agreement considering the different analysis techniques, observation wavelengths, and models adopted by the various studies. We also explored the phase function's dependence on various geologic parameters in a model-independent way. On a global scale, we found that iron abundance and optical maturity (quantified by FeO and OMAT) are the dominant controlling parameters. Titanium abundance (TiO_2), surface roughness on decimeter to decameter scales, and soil thermophysical properties have a smaller effect, but the latter two are correlated with OMAT, indicating that exposure age is the driving force behind their effects. The phase function also exhibited a dependence on slope at ~ 300 m baselines primarily for slopes $\gtrsim 20^\circ$, which is likely due to mass wasting and/or reduced sky visibility. Altogether, compositional variations and space weathering have important effects on the Moon's photometric behavior apart from their influence on single-scattering albedo, a result made possible by LOLA's unique ability to directly measure the normal albedo. Other soil and grain properties, like porosity, roughness, and single particle phase function, are correlated with composition and space weathering.

From a detailed modeling of the photometric function in the Hapke framework, we verified that several geologic influences on the phase function observed by Sato et al. (2014) in the UV-VIS continue into the near-IR. Relative to the highlands, the maria exhibited decreased backscattering (lower c , higher b), a smaller OE width (smaller h_S), and a smaller OE amplitude (smaller B_{S0}). This suggests that the trends of B_{S0} with wavelength that Sato et al. (2014) observed continue into the near-IR. Immature highlands regolith has a higher backscattering fraction and a wider OE width compared to mature highlands regolith. Like Sato et al. (2014), we also found that the Hapke parameters h_S , b , and c have no significant correlation with geologic context within the maria.

The phase difference map revealed additional geologically-influenced variations in the phase function's shape. In particular, variations were observed associated with the dark halo around Jackson crater, the impact ejecta of Copernicus and Giordano Bruno, and the Reiner Gamma Formation. For the latter, we found that the phase function behaves more optically immature than the global phase function for its composition and OMAT, suggesting a difference in how the visible-to-near-IR spectrum and phase function respond to the unusual regolith evolution and properties at this location. Space weathering models could

benefit from using the observed phase function as an additional constraint be-
 920 sides the reflectance spectrum. It is common practice to model the observed
 spectra as mixtures of different endmembers, thereby gaining insight into the
 composition and mineralogy of the regolith. The phase function can provide
 additional information with which to constrain such spectrophotometric inver-
 sion techniques (Mustard and Pieters, 1989; Pilonget et al., 2015; Lucey, 1998;
 925 Clark et al., 2001).

The phase function is a useful tool with which to study the lunar surface,
 but additional work is needed to fully understand how surface properties affect
 its scattering behavior. Spatially resolved studies of the phase function can help
 identify and characterize unique or otherwise interesting geologic features. Laser
 930 altimeters like LOLA can contribute to such studies thanks to their combined
 active and passive radiometry measurements at all phase angles.

10. Acknowledgments

We would like to thank Paul Lucey and Hiro Sato for helpful comments on a
 draft of this paper. We thank Jan McGarry and John Cavanaugh for help with
 935 the LOLA flight software. We also thank the LRO Mission Operations Center
 and LOLA science teams for their hard work in producing the LOLA data used
 in this study.

References

- Bandfield, J.L. et al., 2011. Lunar surface rock abundance and regolith fines
 940 temperatures derived from LRO Diviner Radiometer data. *J. Geophys. Res.:
 Planets* 116, 0. doi:10.1029/2011JE003866.
- Belton, M.J.S. et al., 1994. Galileo multispectral imaging of the north polar
 and eastern limb regions of the Moon. *Science* 264, 1112–1115. doi:10.1126/
science.264.5162.1112.
- 945 Besse, S. et al., 2013a. A visible and near-infrared photometric correction
 for Moon Mineralogy Mapper (M³). *Icarus* 222, 229–242. doi:10.1016/j.
icarus.2012.10.036.
- Besse, S. et al., 2013b. One Moon, many measurements 2: Photometric correc-
 tions. *Icarus* 226, 127–139. doi:10.1016/j.*icarus*.2013.05.009.
- 950 Blewett, D.T. et al., 2011. Lunar swirls: Examining crustal magnetic anomalies
 and space weathering trends. *J. Geophys. Res.: Planets* 116, 2002. doi:10.
 1029/2010JE003656.
- Buratti, B.J. et al., 2011. A wavelength-dependent visible and infrared spec-
 trophotometric function for the Moon based on ROLO data. *J. Geophys. Res.:
 955 Planets* 116, 0. doi:10.1029/2010JE003724.

- Burns, R.G., 1993. Mineralogical Applications of Crystal Field Theory, second ed. Cambridge Univ. Press, Cambridge.
- Byrne, S. et al., 2008. Interannual and seasonal behavior of Martian residual ice-cap albedo. *Planet. Space Sci.* 56, 194–211. doi:10.1016/j.pss.2006.03.018.
- Clark, B.E. et al., 2001. Space weathering on Eros: Constraints from albedo and spectral measurements of Psyche crater. *Meteorit. and Planet. Sci.* 36, 1617–1637. doi:10.1111/j.1945-5100.2001.tb01853.x.
- Cord, A.M. et al., 2003. Planetary regolith surface analogs: optimized determination of Hapke parameters using multi-angular spectro-imaging laboratory data. *Icarus* 165, 414–427. doi:10.1016/S0019-1035(03)00204-5.
- Déau, E. et al., 2013. Re-analysis of previous laboratory phase curves: 1. Variations of the opposition effect morphology with the textural properties, and an application to planetary surfaces. *Icarus* 226, 1465–1488. doi:10.1016/j.icarus.2013.01.014.
- Eliason E. et al., 1999. Mission to the Moon: The Clementine UVVIS Global Lunar Mosaic, PDS Volumes USA-NASA-PDS-CL-4001 through 4078, produced by the U.S. Geological Survey and distributed on CD media by the Planetary Data System, 1999.
- Gaddis, L.R. et al., 1985. Remote sensing of lunar pyroclastic mantling deposits. *Icarus* 61, 461–489. doi:10.1016/0019-1035(85)90136-8.
- Garrick-Bethell, I. et al., 2011. Spectral properties, magnetic fields, and dust transport at lunar swirls. *Icarus* 212, 480–492. doi:10.1016/j.icarus.2010.11.036.
- Gault, D.E. et al., 1974. Mixing of the lunar regolith, in: *Lunar Planet. Sci. Abstracts LPI 5*. 260-262.
- Goguen, J.D. et al., 2010. A new look at photometry of the Moon. *Icarus* 208, 548–557. doi:10.1016/j.icarus.2010.03.025.
- Goossens, S. et al., 2009. Orbit Determination for the Kaguya Satellites: Altimetry Crossovers and Extended Mission Data, presented at the 19th Workshop on JAXA Astrodynamics and Flight Mechanics, Sagamihara, Japan.
- Grier, J.A. et al., 2001. Optical maturity of ejecta from large rayed lunar craters. *J. Geophys. Res.* 106, 32847–32862. doi:10.1029/1999JE001160.
- Hapke, B., 1984. Bidirectional reflectance spectroscopy. III - Correction for macroscopic roughness. *Icarus* 59, 41–59. doi:10.1016/0019-1035(84)90054-X.
- Hapke, B., 2001. Space weathering from Mercury to the asteroid belt. *J. Geophys. Res.* 106, 10039–10074. doi:10.1029/2000JE001338.

- 995 Hapke, B., 2012a. Bidirectional reflectance spectroscopy 7. The single particle
phase function hockey stick relation. *Icarus* 221, 1079–1083. doi:10.1016/j.
icarus.2012.10.022.
- Hapke, B., 2012b. *Theory of Reflectance and Emittance Spectroscopy*, second
ed. Cambridge Univ. Press, Cambridge.
- 1000 Hapke, B. et al., 2012. The wavelength dependence of the lunar phase curve
as seen by the Lunar Reconnaissance Orbiter wide-angle camera. *J. Geo-
phys. Res.: Planets* 117, 0. doi:10.1029/2011JE003916.
- Hapke, B., Sato, H., 2015. The Porosity of the Upper Lunar Regolith, *Lunar
Planet. Sci.* 46, 1216–1217.
- 1005 Hapke, B.W., 1963. A theoretical photometric function for the lunar surface.
J. Geophys. Res. 68, 4571–4586.
- Hare, T.M. et al., 2008. Clementine Mosaics Warped to ULCN2005 Network,
Lunar Planet. Sci. 39, 2337–2338.
- Heiken, G.H., Vaniman, D.T., French, B.M., 1991. *Lunar Sourcebook: A User's
Guide to the Moon*. Cambridge Univ. Press, Cambridge.
- 1010 Helfenstein, P., Shepard, M.K., 1999. Submillimeter-scale topography of the
lunar regolith. *Icarus* 141, 107–131. doi:10.1006/icar.1999.6160.
- Helfenstein, P., Shepard, M.K., 2011. Testing the Hapke photometric model:
Improved inversion and the porosity correction. *Icarus* 215, 83–100. doi:10.
1016/j.icarus.2011.07.002.
- 1015 Hemingway, D.J. et al., 2015. Latitudinal variation in spectral properties of
the lunar maria and implications for space weathering. *Icarus* doi:10.1016/
j.icarus.2015.08.004.
- Hirata, N. et al., 2010. Remote Sensing Study of a Large Lunar Crater Jackson,
Lunar Planet. Sci. 41, 1585–1586.
- 1020 Hood, L.L., Schubert, G., 1980. Lunar magnetic anomalies and surface optical
properties. *Science* 208, 49–51. doi:10.1126/science.208.4439.49.
- Hood, L.L. et al., 2001. Initial mapping and interpretation of lunar crustal mag-
netic anomalies using Lunar Prospector magnetometer data. *J. Geophys. Res.*
106, 27825–27840. doi:10.1029/2000JE001366.
- 1025 Kaydash, V. et al., 2009. Photometric anomalies of the lunar surface studied
with SMART-1 AMIE data. *Icarus* 202, 393–413. doi:10.1016/j.icarus.
2009.03.018.
- Kramer, G.Y. et al., 2011. Characterization of lunar swirls at Mare Ingenii: A
model for space weathering at magnetic anomalies. *J. Geophys. Res.: Planets*
116, 4008. doi:10.1029/2010JE003669.
- 1030

- Kreslavsky, M.A., Shkuratov, Y.G., 2003. Photometric anomalies of the lunar surface: Results from Clementine data. *J. Geophys. Res.: Planets* 108, 5015. doi:10.1029/2002JE001937.
- 1035 Kreslavsky, M.A. et al., 2000. Photometric properties of the lunar surface derived from Clementine observations. *J. Geophys. Res.* 105, 20281–20296. doi:10.1029/1999JE001150.
- Lagarias, J.C., 1998. Convergence properties of the nelder–mead simplex method in low dimensions. *SIAM J. on Optimization* 9, 112–147. doi:10.1137/S1052623496303470.
- 1040 Lemoine, F.G. et al., 2014. GRGM900C: A degree 900 lunar gravity model from GRAIL primary and extended mission data. *Geophys. Res. Lett.* 41, 3382–3389. doi:10.1002/2014GL060027.
- Lucey, P. et al., 2006. Understanding the Lunar Surface and Space-Moon Interactions. *Rev. Mineral. Geochem.* 60, 83–219.
- 1045 Lucey, P.G., 1998. Model near-infrared optical constants of olivine and pyroxene as a function of iron content. *J. Geophys. Res.* 103, 1703. doi:10.1029/97JE03145.
- Lucey, P.G. et al., 2000a. Lunar iron and titanium abundance algorithms based on final processing of Clementine ultraviolet-visible images. *J. Geophys. Res.* 105, 20297–20306. doi:10.1029/1999JE001117.
- 1050 Lucey, P.G. et al., 2000b. Imaging of lunar surface maturity. *J. Geophys. Res.* 105, 20377–20386. doi:10.1029/1999JE001110.
- Lucey, P.G. et al., 1986. A compositional study of the aristarchus region of the moon using near-infrared reflectance spectroscopy. *J. Geophys. Res.* 91, D344–D354. doi:10.1029/JB091iB04p0D344.
- 1055 Lucey, P.G. et al., 2014. The global albedo of the Moon at 1064 nm from LOLA. *J. Geophys. Res.: Planets* 119, 1665–1679. doi:10.1002/2013JE004592.
- Mao, D. et al., 2013. Laser Ranging to the Lunar Reconnaissance Orbiter: improved timing and orbits. *AGU Fall Meeting Abstracts*, B1748.
- 1060 Mazarico, E. et al., 2013. Improved Precision Orbit Determination of Lunar Orbiters from the GRAIL-derived Lunar Gravity Models, in: 23rd AAS/AIAA Space Flight Mechanics Meeting, pp. 13–274.
- McEwen, A.S., 1996. A Precise Lunar Photometric Function. *Lunar Planet. Sci.* 27, 841–842.
- 1065 McEwen, A.S. et al., 1993. Galileo observations of post-imbrium lunar craters during the first Earth-Moon flyby. *J. Geophys. Res.* 98, 17207–17234. doi:10.1029/93JE01137.

- McGuire, A.F., Hapke, B.W., 1995. An experimental study of light scattering by large, irregular particles. *Icarus* 113, 134–155. doi:10.1006/icar.1995.1012.
- 1070 Mitrofanov, I.G. et al., 2007. Water ice permafrost on Mars: Layering structure and subsurface distribution according to HEND/Odyssey and MOLA/MGS data. *Geophys. Res. Lett.* 34, 18102. doi:10.1029/2007GL030030.
- Mustard, J.F., Pieters, C.M., 1989. Photometric phase functions of common geologic minerals and applications to quantitative analysis of mineral mixture reflectance spectra. *J. Geophys. Res.* 94, 13619–13634. doi:10.1029/JB094iB10p13619.
- 1075 Nelson, D.M. et al., 2014. Mapping Lunar Maria Extents and Lobate Scarps Using LROC Image Products. *Lunar Planet. Sci.* 45, 2861-2862.
- Neumann, G.A. et al., 2015. Copernican-Age Craters and LOLA Decameter-Scale Roughness. *Lunar Planet. Sci.* 46, 2218-2219.
- 1080 Ohtake, M. et al., 2010. Deriving the absolute reflectance of lunar surface using SELENE (Kaguya) Multiband Imager data. *Space Sci. Rev.* 154, 57–77. doi:10.1007/s11214-010-9689-0.
- Pieters, C.M. et al., 2013. One Moon, many measurements 1: Radiance values. *Icarus* 226, 951–963. doi:10.1016/j.icarus.2013.07.008.
- 1085 Pilorget, C. et al., 2015. Photometry of particulate mixtures: What controls the phase curve? *Icarus* 250, 188–203. doi:10.1016/j.icarus.2014.11.036.
- Pinet, P.C. et al., 2000. Local and regional lunar regolith characteristics at Reiner Gamma Formation: Optical and spectroscopic properties from Clementine and Earth-based data. *J. Geophys. Res.* 105, 9457–9476. doi:10.1029/1999JE001086.
- 1090 Sato, H. et al., 2014. Resolved Hapke parameter maps of the Moon. *J. Geophys. Res.: Planets* 119, 1775–1805. doi:10.1002/2013JE004580.
- Shepard, M.K., Helfenstein, P., 2007. A test of the Hapke photometric model. *J. Geophys. Res.: Planets* 112, 3001. doi:10.1029/2005JE002625.
- 1095 Shkuratov, Y. et al., 2003. Classical photometry of prefractal surfaces. *J. Opt. Soc. Am. A* 20, 2081–2092. doi:10.1364/JOSAA.20.002081.
- Shkuratov, Y.G. et al., 1999. Opposition effect from Clementine data and mechanisms of backscatter. *Icarus* 141, 132–155. doi:10.1006/icar.1999.6154.
- 1100 Smith, D.E. et al., 2010a. The Lunar Orbiter Laser Altimeter Investigation on the Lunar Reconnaissance Orbiter Mission. *Space Sci. Rev.* 150, 209–241. doi:10.1007/s11214-009-9512-y.

- Smith, D.E. et al., 2010b. Initial observations from the Lunar Orbiter Laser Altimeter (LOLA). *Geophys. Res. Lett.* 37, L18204. doi:10.1029/2010GL043751.
- 1105 Souchon, A.L. et al., 2013. Local spectrophotometric properties of pyroclastic deposits at the Lavoisier lunar crater. *Icarus* 225, 1–14. doi:10.1016/j.icarus.2013.03.004.
- Souchon, A.L. et al., 2011. An experimental study of Hapke’s modeling of natural granular surface samples. *Icarus* 215, 313–331. doi:10.1016/j.icarus.2011.06.023.
- 1110 Sun, X. et al., 2006. Mars 1064 nm spectral radiance measurements determined from the receiver noise response of the Mars Orbiter Laser Altimeter. *Appl. Opt.* 45, 3960–3971. doi:10.1364/AO.45.003960.
- 1115 Yamamoto, S. et al., 2011. Preflight and in-flight calibration of the Spectral Profiler on board SELENE (Kaguya). *IEEE Trans. Geosci. Remote Sens.* 49, 4660–4676. doi:10.1109/TGRS.2011.2144990.
- Yokota, Y. et al., 2011. Lunar photometric properties at wavelengths 0.5–1.6 μm acquired by SELENE Spectral Profiler and their dependency on local albedo and latitudinal zones. *Icarus* 215, 639–660. doi:10.1016/j.icarus.2011.07.028.
- 1120 York, D. et al., 2004. Unified equations for the slope, intercept, and standard errors of the best straight line. *Am. J. Phys.* 72, 367–375. doi:10.1119/1.1632486.
- 1125 Zuber, M.T. et al., 2013. Gravity Field of the Moon from the Gravity Recovery and Interior Laboratory (GRAIL) Mission. *Science* 339, 668–671. doi:10.1126/science.1231507.
- Zuber, M.T. et al., 2010. The Lunar Reconnaissance Orbiter laser ranging investigation. *Space Sci. Rev.* 150, 63–80. doi:10.1007/s11214-009-9511-z.